

1  
2  
3  
4  
5  
6  
7  
8  
9  
10  
11  
12  
13  
14  
15  
16  
17  
18  
19  
20  
21  
22  
23  
24  
25  
26  
27  
28  
29  
30  
31  
32  
33  
34  
35  
36  
37  
38

**REVISION 2**

**Aluminum and iron behavior in glasses from destabilized spinels: a  
record of fluid/melt-mineral interaction in mantle xenoliths from  
Massif Central, France.**

**MICHEL FIALIN<sup>1,\*</sup> AND CHRISTIANE WAGNER<sup>2,3</sup>**

<sup>1</sup>Centre de Microanalyse Camparis, UPMC Univ Paris 06, IPGP, CNRS-UMR  
7094, F-75005, Paris, France

<sup>2</sup>Sorbonne Universités, UPMC Univ Paris 06, UMR 7193, ISTeP, F-75005, Paris,  
France

<sup>3</sup>CNRS, UMR 7193, ISTeP, F-75005, Paris, France

\* Corresponding author. [michel.fialin@upmc.fr](mailto:michel.fialin@upmc.fr)

**ABSTRACT**

Infiltrations of melts (and/or fluids) in mantle rocks are witnessed by the presence of glass-bearing pockets in peridotite xenoliths brought to the surface by alkaline volcanism. Several glass-bearing pockets found around spinels corroded at different degrees were investigated for their chemical compositions, including the  $\text{Fe}^{3+}/\Sigma\text{Fe}$  ratios, in two xenolith samples by electron probe microanalysis. The dissolution/recrystallization of spinels enriches the melt in alumina. We show that the spinel-derived  $\text{Al}^{3+}$  ions could have been accommodated to the melt network first as network-modifiers. Then  $\text{Al}^{3+}$  ions were network-formers using  $\text{K}^+$  ions, extracted from the aqueous fluid upon melt dehydration, as stabilizers within the tetrahedral site. The transfer of  $\text{K}^+$  from the aqueous fluid to the melt network is counterbalanced by an inverse transfer of  $\text{CaO}$  molecules that form crystalline phases exsolved upon eruption. The evolution of the Al content clearly shows that an increasing fraction of the spinel-derived alumina molecules were exsolved as the melt dehydration proceeded. Spinel corrosion could also be at the origin of melt oxidation through dehydrogenation reactions resulting in the formation of  $\text{Al}^{3+}$  and  $\text{Fe}^{3+}$  anionic complexes within the melt

39 network. This study shows (1) how the structure of the percolating melt is modified by  
40 the accommodation of chemical elements produced by the dissolution of minerals and  
41 (2) how this process could modify the oxidation state of the melt.

42 **Keywords:** Silicate melt, mantle xenoliths, electron microprobe,  $\text{Fe}^{3+}/\Sigma\text{Fe}$   
43 measurements, melt/fluid-spinel interactions.

44  
45  
46  
47

## INTRODUCTION

48 Glass-bearing reaction textures are world-wide known in mantle xenoliths.  
49 They usually consist of sieve-textured rims on clinopyroxene and spinel, reaction  
50 rims on orthopyroxene and reaction pockets developed around amphibole and spinel.  
51 Besides patches of glass, the pocket assemblage contains secondary small crystals of  
52 olivine, clinopyroxene and spinel. The textural and chemical characteristics of the  
53 reaction zones have been considered as important clues for elucidating the origin of  
54 the associated glass, and intensively studied over the past two decades. However, the  
55 interpretation of the reaction textures remains controversial as it is difficult to  
56 unequivocally determine the processes and timing of their formation. Two main  
57 opposite interpretations have been argued considering the reaction textures either as  
58 products of mantle processes or resulting from reactions posterior to the xenolith  
59 entrainment in its host magma. Partial melting may have occurred in the mantle  
60 induced by heating (e.g. Maaloe and Printzlau, 1979) or decompression (e.g. Su et al.  
61 (2011). It may also result from the percolation of fluids (e.g. Carpenter et al., 2002;  
62 Coltorti et al., 2000), or invading melt (e.g. Perinelli et al., 2008 and papers in  
63 Coltorti and Grégoire, 2008). In contrast, these textures may have developed in  
64 crustal magma chambers or during the xenolith transport to the surface by  
65 decompression-induced partial melting, or reactions with the magma host (e.g.  
66 Carpenter et al., 2002; Shaw et al., 2006 and references therein; Wang et al., 2012).  
67 In hydrous xenoliths, the reaction textures may also have developed after the  
68 incongruent breakdown of amphibole in the mantle or during transport (e.g. Shaw  
69 and Klügel, 2002; Ban et al., 2005; Ismail et al., 2008; Shaw, 2009).

70 We present here a detailed investigation of fresh glass patches preserved in  
71 reaction textures (from few tens  $\mu\text{m}^2$ - to  $\text{mm}^2$ -sized) in two lherzolite xenoliths - one  
72 anhydrous and one hydrous - from the French Massif Central. The aim of this study  
73 is to examine the exchanges, involving Al and Fe particularly, between the melt/fluid

|

74 and the peridotite minerals by the means of an electron microprobe (EMP)  
75 investigation, including the measurements of the  $\text{Fe}^{3+}/\Sigma\text{Fe}$  ratios.

76  
77

## 78 **GEOLOGICAL OUTLINES**

79

80 The French Massif Central is part of the Variscan belt in Western Europe. It  
81 shows an intense Cenozoic alkaline volcanism linked to the upwelling of mantle  
82 material, possibly related to a hotspot or to channelling of asthenospheric material  
83 through lithospheric fractures (e.g. Granet et al., 1995; Hoernle et al., 1995; Granet et  
84 al., 2000). Two distinct lithospheric domains situated north and south of the 45°30'N  
85 parallel have been recognized: protogranular refractory peridotites are found in the  
86 northern domain, and fertile coarse-granular peridotites in the southern domain (as  
87 defined by Lenoir et al., 2000; see also Downes et al., 2003). Melts and fluids  
88 emanating from the mantle upwellings have greatly modified the underlying lithosphere  
89 (e. g. Downes and Dupuy, 1987; Wilson and Downes, 1991; Vanucci et al., 1994;  
90 Zangana et al., 1997; Xu et al., 1998; Lenoir et al., 2000; Downes et al., 2003; Féménias  
91 et al., 2004).

92 Our study focuses on the Devès area which belongs to the southern lithospheric  
93 domain, near the limit between the two domains mentioned above. The Devès volcanic  
94 field is a basaltic plateau that hosted more than 150 volcanic cones aligned along a  
95 NNW-SSE trend. The volcanism is younger than 4 Ma (Maury and Varet, 1980) and  
96 consists mainly of basanites (see the detailed review of the Devès volcanism by Mergoïl  
97 and Boivin, 1993). The Devès underlying mantle has been intensively percolated by  
98 hydrous alkaline melts leading to the crystallization of metasomatic minerals,  
99 amphibole, mica and clinopyroxene, as well as cryptic metasomatism (Lenoir et al.,  
100 2000; Touron et al., 2008; Wagner and Deloule, 2007).

101

102

103

## 103 **PETROGRAPHY OF THE XENOLITHS**

104

105 The xenoliths come from the consolidated scoriae cone of Mont Gros (quoted as  
106 MG below) near Alleyras (N44°54', E3°41'). The xenolith-entraining magma is a Si-  
107 undersaturated alkaline basanite (Jardin, 1973). We have collected 150 ultramafic  
108 xenoliths and discarded any xenoliths with dusty olivine and pyroxene or showing

109 oxidation due to heating by the host magma. The dominant petrologic type is a spinel  
110 lherzolite which contains amphibole in 20% of the xenoliths. Amphibole is a pargasite  
111 that forms either disseminated crystals interstitial to olivine, clinopyroxene,  
112 orthopyroxene and spinel, or developed around spinels, whereas an amphibole selvage  
113 that partially surrounded the peridotite is sometimes observed. Half of the spinel  
114 lherzolite xenoliths show glassy percolation paths of an invading melt/fluid and glass-  
115 bearing reaction pockets. The reaction pockets are either interstitial or developed around  
116 spinel ± amphibole. It should be noticed that in half of the amphibole-bearing xenoliths,  
117 amphibole is not surrounded by a reaction pocket. For this study we focus on two spinel  
118 lherzolite xenoliths: anhydrous sample MG102 and sample MG54 with relicts of  
119 amphibole. Both samples are planar-faced fresh xenoliths of ~ 10 cm in diameter with  
120 remnants of a vesicular basanite crust (Figs. 1 and 2). They show glass-bearing reaction  
121 zones often located around spinel or disseminated in the lherzolite. A detailed  
122 petrographic description of the two samples is given in Appendix A.

123 In the following, “secondary” referred to the neoformed phases observed in the  
124 reaction pockets, and “primary” to the original phases of the lherzolite. In sample  
125 MG102 reaction features are observed at the contact with the host basanite (Fig. 1):  
126 orthopyroxene shows dissolution along former cleavages (Fig. 1d) and clinopyroxene  
127 has a sieve texture, which may invade the whole grain (Fig. 1b). Close to the contact  
128 with the host basanite spinel develops a thick (up to 700 μm) zone of opaque spinel  
129 surrounding the brown core (Fig. 1e, zone 1) and is embedded in a large vesicular glass-  
130 bearing reaction zones including secondary olivine and clinopyroxene. Glass-bearing  
131 reactional paths penetrate the xenolith from the contact with the basanite (Fig. 1b).  
132 However, no such intense interaction can be evidenced further inside the xenolith  
133 (zones 3 and 4) as clinopyroxene is not sieve-textured and spinel poorly corroded (Fig.  
134 1f) or uncorroded (Fig. 1g). Sample MG54 shows no evidence of reaction with the host  
135 basanite and no glass-bearing reactional paths throughout the xenolith (Fig. 2). The  
136 glass-bearing reaction zones only occur around spinel (Fig. 2) and show relicts of  
137 amphibole in some locations (Fig. 2d).

138

### 139 **Detailed description of reaction zones around corroded spinels**

140 Figures 3 to 6 show typical reaction zones in the MG54 and MG102 samples,  
141 featured by the backscattered (BSE) images as well as the elemental maps of Al, alkalis,  
142 Ca and Mg expressed as oxide-wt.%. The reaction zones developed around primary

143 spinel in contact with primary orthopyroxene. Primary spinel exhibits a sieve-textured  
144 rim consisting of small secondary spinel grains in a glass framework that embeds  
145 secondary olivine and clinopyroxene. We note first in the BSE images the presence of  
146 abundant bubble-like voids (black) corresponding to formerly volatile- filled vesicles  
147 that formed at low pressure or upon eruption. The presence of former H<sub>2</sub>O-rich (instead  
148 of CO<sub>2</sub>-rich) fluid is likely as amphibole is present in numerous Mont Gros lherzolite  
149 samples (see above).

150 In sample MG54, spinel appears as white shades in the BSE image (Fig. 3a and b)  
151 and orange in the Al<sub>2</sub>O<sub>3</sub> map (Fig. 3c). The residual melt forms a connected framework,  
152 blue-green in the Al<sub>2</sub>O<sub>3</sub> map (Fig. 3c) and white in the Na<sub>2</sub>O + K<sub>2</sub>O map (Fig. 3e). In  
153 sample MG102 the primary spinels from zone 4 exhibit a very limited sieve-textured  
154 rim around a corroded core (Fig. 4) and are surrounded by poorly developed reaction  
155 zones (Fig. 4a) similar to those of sample MG54. However, in contrast to sample  
156 MG54, the major feature of sample MG102 is the large degree of corrosion of the  
157 primary spinel evidenced in some locations, e.g. zone 1 (Figs. 1c, e; Fig. 5a - c). The  
158 core of the relict primary spinel exhibits large corrosion induced embayments and  
159 perforations (red arrows in Fig. 5b). The highly corroded rim shows development of a  
160 large amoeboid-shaped spongy corona consisting of numerous small secondary Al-rich  
161 spinel grains (white-green-red in Fig. 5c) embedded in a dense glass framework (green  
162 in Fig. 5c, white in Fig. 5e). Moreover, in some locations of the MG102 sample,  
163 primary spinels are no longer observed and only few blebs of secondary spinel still  
164 remain visible (Fig. 1c, zone 2, Fig. 6).

#### 165 166 167 **ANALYTICAL PROCEDURE** 168

169 High spatial resolution BSE images were obtained with a Carl Zeiss Supra 55VP  
170 field-emission scanning electron microscope (FE-SEM). The analyses of hematite and  
171 magnesioferrite in Table 3 were performed using the energy dispersive spectrometer  
172 (EDS) attached to the FE-SEM. The chemical composition of the other minerals and  
173 glasses, as well as the glass Fe<sup>3+</sup>/ΣFe ratios, were determined with a Cameca SXFive  
174 electron microprobe equipped with five wavelength dispersive spectrometers (WDS).  
175 Three of the WDS were equipped with TAP monochromators (two regular -660 mm<sup>2</sup>-  
176 TAP and one large-area -1320 mm<sup>2</sup>- TAP) to collect the Fe-Lα peak data that are used

177 by the procedure for the determination of the  $\text{Fe}^{3+}/\Sigma\text{Fe}$  ratios as explained hereafter.  
178 Both EDS and WDS analyzes were performed using the following standards: diopside  
179 for Si, Mg and Ca; orthose for Al and K; albite for Na; apatite Durango for P;  $\text{MnTiO}_3$   
180 for Mn and Ti; hematite for Fe; scapolite for Cl; topaz for F.

181 The determination of the  $\text{Fe}^{3+}/\Sigma\text{Fe}$  ratios, known as the ‘peak shift’ method is  
182 detailed in Fialin et al. (2001, 2004, and 2011) and can be summarized as follows. First,  
183 each glass analysis presented in Table 2 represents the average of ten neighboring  
184 locations probed with a 15 kV, 10 nA and 20  $\mu\text{m}$  beam at a single glass pocket. The  
185 dwell time for each element was 10s on peaks plus 10s on backgrounds. Second, the  
186 wavelength positions of the  $\text{Fe-L}\alpha$  peak, necessary for  $\text{Fe}^{3+}/\Sigma\text{Fe}$  ratios determination,  
187 were measured on each of the ten locations with the same spot beam conditions except  
188 for the intensity that was increased to 80 nA. We thus obtained a single  $\text{Fe}^{3+}/\Sigma\text{Fe}$  value  
189 per glass pocket investigated. We carefully checked for the common pitfalls encountered  
190 with the use of the peak shift method applied to glasses, particularly, i.e. the roles played  
191 in the position shift of the  $\text{FeL}\alpha$  peak by (1) beam induced oxidation and (2) matrix  
192 effects. (1) Beam induced oxidation causes the shift of the  $\text{FeL}\alpha$  peak toward lower  
193 wavelength with subsequent increase of  $\text{Fe}^{3+}/\Sigma\text{Fe}$ . In order to overcome this difficulty,  
194 eight replicate measurements of the peak position were performed at each of the ten  
195 glass locations. The ‘true’ peak position was evaluated as the zero time intercept of the  
196 branch of parabola fitting the eight values (refer to figures 6 and 7 in Fialin et al, 2001  
197 and figure 5 in Fialin et al, 2004, for examples). (2) The composition of the studied  
198 glasses is similar to those of the standards used to construct the calibration curves,  
199 which allows avoiding any  $\text{FeL}\alpha$  peak shift due to matrix effects (refer to the extended  
200 discussion in Fialin et al, 2001, paragraph “Limitation” p. 462).

201 |  
202

## 203 | CHEMICAL RESULTS

204

205 We focus below on the composition of spinel and glass from the reaction pockets,  
206 whereas a summary of the chemical composition of the primary and secondary silicate  
207 minerals is given in Appendix 2.

208 **Spinel**

|

209           The compositions of the spinels in both MG54 and MG102 samples are given in  
210 Table 1. Marked compositional differences between uncorroded primary spinel cores  
211 and secondary spinel are observed: for example in sample MG54, secondary spinel is  
212 Cr<sub>2</sub>O<sub>3</sub> enriched (17.3 – 25.3 wt. %) and Al<sub>2</sub>O<sub>3</sub> depleted (43.6 – 51.0 wt. %) compared to  
213 primary spinels (13.9 – 16.5 wt. % Cr<sub>2</sub>O<sub>3</sub> and 50.3 – 53.0 wt. % Al<sub>2</sub>O<sub>3</sub>). These  
214 differences are dramatically increased for the highly corroded spinels in zones 1 and 2  
215 of the MG102 sample, which have a variable and extremely high cr\* (21.3 - up to 63.4  
216 in zone 2).

217

### 218 **Glass**

219           The glasses are alkali-rich and Si-saturated or oversaturated, except the glasses  
220 from the two most destabilized zones 1 and 2 of MG102, which are Si-undersaturated  
221 (11% and 5 % normative nepheline, respectively; Table 2). The TAS (total alkali -  
222 silica) diagram (Fig. 7) shows that glasses from MG54 have a restricted range of  
223 composition compared to those of sample MG102, in which glasses from zones 1 and 2  
224 reach a trachytic composition. Such glasses are world-wide known in mantle xenoliths  
225 (Coltorti and Grégoire, 2008). In sample MG102 the glass from the two reaction  
226 pockets with highly corroded spinels from zones 1 and 2 shows high silica and alkali  
227 compared to the pockets from the zones 3 and 4, in which spinel is poorly corroded  
228 (Table 2; Fig. 7). The glasses from zones 3 and 4 have a composition similar to that of  
229 the glasses from MG54, but Al- and Fe<sup>3+</sup>-richer and K-depleted (Fig. 8). Glasses from  
230 sample MG54 and zones 3 and 4 of sample MG102 contain between 3.6 - 4.7 wt.%  
231 MgO , while glasses associated with highly corroded spinels (MG102, zones 1 and 2)  
232 are less magnesian (~2 wt.% MgO).

233

234

235

## 235 **DISCUSSION**

236

### 237 **Origin of the glassy pockets**

238           Before discussing the behavior of aluminum and iron in glass from the reaction  
239 pockets around spinel, we first examine the glass origin. The xenoliths display  
240 distinct reaction features suggesting different genetic processes that are discussed  
241 below based on the previously exposed textural and chemical characteristics of the  
242 reaction zones and compared to experimental results.

|

243           **Xenolith - host magma interaction after entrainment.** Some features are  
244 clearly related to interaction between the xenolith and the host magma. In sample  
245 MG102, the most corroded spinels are observed in the reaction zones 1 and 2 close to  
246 the contact with the basanite host (Fig. 1). The composition of the associated glass (ne-  
247 normative) is quite distinct from that of glasses (Si-saturated or oversaturated) from  
248 reaction zones further inside the xenolith (Table 2), where no host melt percolation was  
249 observed. Its composition matches that of experimental melts obtained by incongruent  
250 dissolution of orthopyroxene in Si-undersaturated alkaline melt at one atmosphere  
251 (Shaw et al., 1998; Shaw and Dingwell, 2008). In these experiments, the dissolution of  
252 orthopyroxene is followed by the crystallization of new olivine + clinopyroxene from  
253 the boundary layer melt. According to these authors, clinopyroxene likely results from a  
254 local clinopyroxene saturation after the diffusion of calcium towards the orthopyroxene.  
255 In sample MG102 secondary clinopyroxene crystals are indeed concentrated close to the  
256 primary orthopyroxene (Figs. 5 and 6). Moreover, the reaction zones contain a high  
257 amount of olivine (Figs. 3 - 6), a fact mentioned in experimental studies (Shaw et al.,  
258 1998; Shaw, 1999) in relation to the alkali-rich character of the reacting infiltrating  
259 melt, which stabilized olivine (Kushiro, 1975). The melt produced by the incongruent  
260 dissolution of orthopyroxene causes then the destabilization of spinel (e.g. as proposed  
261 by Shaw and Dingwell, 2008), and the crystallization of Cr-richer secondary spinel in  
262 the destabilized rim (Table 1). The influence of the host magma seems to be limited to  
263 the vicinity of the contact with the xenolith, as the interior of the xenolith shows no  
264 traces of percolation of the host magma and no sieve-textured clinopyroxene (Fig. 1),  
265 while the reaction zones around spinel (e.g. zones 4 in sample MG102, Fig. 1f) are less  
266 developed with a glass of quite different composition (Table 2). Other mechanisms are  
267 thus required in both samples for the formation of reaction zones away from host melt  
268 influence.

269           **In situ and decompression melting.** Silicic and alkaline liquids may be obtained  
270 by low-degree disequilibrium melting in the mantle at P about 1-1.5 GPa (Draper and  
271 Green, 1999; Lo Cascio et al., 2008). These experimental liquids are anhydrous, sodic,  
272 potassic (Draper and Green, 1999) or not potassic (Lo Cascio et al., 2008), and Si-  
273 undersaturated. In contrast MG102 glasses from the reaction zones 3 and 4 (located in  
274 the interior of the xenolith) are Si-saturated or -oversaturated, and, thus, not consistent  
275 with small degrees of in situ partial melting of the lherzolite. On the other hand,  
276 although lherzolite xenoliths are abundant in the Mont Gros occurrence, only about half



277 of them show glass-bearing reaction pockets or glass veins. This suggests that  
278 | decomposition melting is not the main - or single - mechanism responsible for the  
279 formation of the reaction zones.

280 **Breakdown of amphibole.** About half of the amphibole-bearing xenoliths from  
281 Mont Gros show reaction zones around amphibole. The formation of glass by  
282 decompression-induced breakdown of amphibole has been proposed by several authors  
283 (e.g. Frey and Green, 1974; Francis, 1976; Stosch and Seck, 1980; Chazot et al., 1996;  
284 Yaxley et al., 1997; Ismail et al., 2008). In sample MG54, small amphibole crystals in  
285 the reaction zones are likely relicts of former destabilized amphibole (Fig. 2d). The glass  
286  $\text{FeO}_{\text{Total}} / \text{MgO}$  ratio (0.8 compared to 0.3 for the amphibole) is consistent with the  
287 ensuing fractional crystallization of Mg-richer secondary olivine, clinopyroxene and  
288 spinel in the reaction zones. The glass is enriched in alkalis compared to the amphibole  
289 with variable but high  $\text{Na}_2\text{O}$  contents (up to 5.0 wt. %), a content higher than that  
290 expected from the crystallization of secondary clinopyroxene after the amphibole  
291 breakdown. This suggests the addition of a Na-rich melt (or fluid?) of untraceable  
292 origin, which may have induced - or contributed to - the melting of pre-existing  
293 amphibole. The melting of amphibole may have occurred either in the mantle before or  
294 during the entrainment of the xenolith in the host magma, but at present we cannot  
295 | argue further on this point. The resulting melt reacts then with the primary minerals in a  
296 manner similar to that described above for the role of the host magma. Lastly, although  
297 amphibole has not been found in sample MG102, amphibole may have completely  
298 melted and its involvement in the formation of the glass cannot be discarded. Moreover,  
299 even if amphibole is involved, the glass high  $\text{Na}_2\text{O}$  content (5.4 - 6.4 wt. %) requires the  
300 contribution of a Na-rich agent, as proposed above for sample MG54. The infiltration is  
301 likely to have occurred shortly before eruption, as a melt fraction was preserved in the  
302 reaction pockets and as there is no diffusion (at the micron scale) in the primary  
303 minerals adjacent to the pockets.

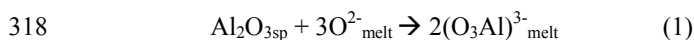
304  
305

306 **Dissolution-crystallization mechanism of spinels: the fate of the spinel-derived**  
307 | **alumina.**

308  
309 As discussed above, melts (now glasses) found in xenoliths have different origins  
310 involving infiltration of melt/fluid and dissolution of primary silicates including  
311 amphibole, followed by the destabilization of spinel. Spinel experienced thus a late

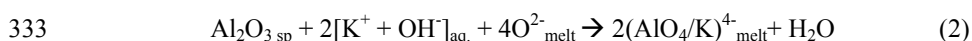
312 corrosion within a preexisting - likely hydrous - silicate melt. The secondary spinels that  
313 crystallized at the periphery of primary spinels are depleted in  $\text{Al}_2\text{O}_3$  (Table 1), with  
314 subsequent Al-enrichment of the silicate melt.

315 **Sample MG54.** We can observe a weak increase of Al with decreasing Mg (Fig.  
316 8). This can be interpreted as reflecting the accommodation of the spinel-derived  $\text{Al}_2\text{O}_3$   
317 molecules to the melt network according to the proposed reaction 1:



319 The accommodation process proceeds necessarily through the breaking of a number of  
320 bonds of the silicate melt network. In reaction 1, three  $\equiv\text{Si}-\text{O}-\text{Si}\equiv$  covalent bonds are  
321 broken (the bond breaking is noted here as the consumption of three bridging oxygens,  
322  $\text{O}_{\text{melt}}^{2-}$ ) and both spinel-derived  $\text{Al}^{3+}$  ions are found as network-modifiers of the melt  
323 network. Two network-modifying units, (noted  $(\text{O}_3\text{Al})^{3-}$ , where  $\text{Al}^{3+}$  neutralizes three  
324 non-bridging oxygens), are consequently formed.

325 **Sample MG102.** Unlike in sample MG54, Al and Mg are here positively  
326 correlated and we also note an important increase of the K concentration with  
327 decreasing Mg, the lowest K concentration, at Mg ~ 2.1 at%, being four times lower in  
328 sample MG102 than in sample MG54 (Fig. 8). This can be interpreted as follows: the  
329 first  $\text{Al}_2\text{O}_3$  molecules released from the dissolution of the MG102 spinels were  
330 essentially accommodated to the melt network after reaction 1. With the on-going  
331 dissolution of spinel, more and more  $\text{Al}_2\text{O}_{3\text{sp}}$  molecules were produced, which were  
332 accommodated to the melt network after the proposed reaction 2:

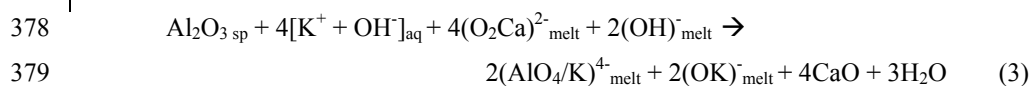


334 The preceding reaction depicts how  $\text{K}^+$  cations were extracted from a KOH phase,  
335 (noted  $[\text{K}^+ + \text{OH}^-]_{\text{aq}}$ ), to stabilize  $\text{Al}^{3+}$  in the tetrahedral site, noted  $(\text{AlO}_4/\text{K})_{\text{melt}}^{4-}$ . The  
336 presence of KOH-like complexes was suggested by Mysen and Acton (1999) in  
337 hydrated melts in the  $\text{K}_2\text{O}-\text{Al}_2\text{O}_3-\text{SiO}_2-\text{H}_2\text{O}$  system. The proposed present reaction 2 is  
338 just the right-to-left direction of reaction 3 found in Mysen and Acton (1999). The latter  
339 study supports the existence of a free aqueous fluid phase in addition to the melt in  
340 alkali aluminosilicate aqueous fluids. KOH complexes are unattached to the melt  
341 network and are probably part of the free aqueous phase. Dissolved  $\text{H}_2\text{O}$  in silicate  
342 melts is generally found as (nano-) phases disseminated throughout the melt network  
343 (e.g. Balcone-Boissard et al., 2009). However, given that water is mostly  
344 accommodated as bonded hydroxyls in basaltic melts (e.g. Lesne et al., 2010), it is  
345 likely that the KOH-bearing aqueous phase was reduced to a brine in our pre-erupted

346 melts. Upon eruption, potassium ions were more and more easily extracted from KOH  
347 as they were more and more dissociated with increasingly rehydrated brine. Note also  
348 that  $K^+$  is the preferred stabilizing ion in the tetrahedral site (e.g. Bottinga and Weill,  
349 1972; Pichavant et al., 1992 and reference therein) and thus, its extraction from the  
350 aqueous fluid predominates over the extraction of other alkalis such as Na. The breaking  
351 of four  $O_{melt}^{2-}$  is also required.

352 The evolutions of K and Al in both melts are schematically represented in figure  
353 9. The pressure-induced injection of the melt in the xenolith led to the corrosion of  
354 spinels accompanied by the release (dotted line) and the accommodation (full lines) of  
355  $Al_2O_{3sp}$  molecules after reactions 1 (dotted-dashed lines) and 2 (dashed lines). Reaction  
356 1 dominates in the first stages of the accommodation process (few  $K^+$  aqueous  
357 fluid  $\rightarrow$  melt transfer). Reaction 2 becomes then more and more efficient which is  
358 recorded as increasing K contents in melt networks with dropping Mg values. As Mg  
359 drops, the proposed mechanism results in an increasing gap between  $Al_2O_{3sp}$  molecules  
360 produced and accommodated to the melt network. As spinel corrosion proceeds with  
361 dehydration, more and more  $Al_2O_{3sp}$  molecules together with  $H_2O$  molecules are  
362 produced, which results in (i) more and more  $Al_2O_{3sp}$  molecules to be transferred into  
363 the aqueous fluid and later exsolved, but in the same time (ii) more and more  $(AlO_4/K)^{4-}_{melt}$   
364 formed through reaction 2. The peculiar point where the Al content is dropping  
365 together with the increase of the K content can be seen in MG54 (Fig. 8). It corresponds  
366 presumably to the beginning of the dehydration process.

367 However, as shown on figure 10, the melt/aqueous fluid exchanges are more  
368 complicated than those depicted in reaction 2. The amount of K extracted from the  
369 aqueous phase is exactly compensated by an amount of Ca that was likely transferred in  
370 the aqueous phase from the melt network, where Ca is known acting as a network-  
371 modifier (Fig. 10a). In addition the rate of variation of the K amount transferred from  
372 the aqueous phase is *ca.* two times higher than that of the amount of spinel-derived Al  
373 accommodated in the melt network (Fig. 10b). Given that only a fraction of this Al is  
374 found in tetrahedral position with K as the stabilizer (Fig. 9), more K than necessary is  
375 extracted from the aqueous phase, which is in contradiction with reaction 2 (that depicts  
376 the common case where one K is required per  $AlO_4$  to be stabilized). The following  
377 dehydration reaction 3 may resume these observations:



380 Where  $(\text{O}_2\text{Ca})_{\text{melt}}^{2-}$  represents a network-modifying unit consisting of a  $\text{Ca}^{2+}$  ion  
381 neutralizing two non-bridging oxygens. Most CaO molecules produced were likely  
382 exsolved with  $\text{H}_2\text{O}$  upon eruption. Finally, two non-bridging oxygens formerly  
383 neutralized by two protons (forming a pair of bonded hydroxyls,  $2(\text{OH})_{\text{melt}}^-$ ) become  
384 now neutralized by two  $\text{K}^+$  extracted from the aqueous phase. The major difference  
385 between reactions 2 and 3 is that no energy-consuming breaking of covalent bonds is  
386 required for reaction 3 in which sole network-modifying units are involved as reactants  
387 to result in a more polymerized melt.

388

### 389 **$\text{Fe}^{2+}$ oxidation**

390 Glasses from the reaction pockets of sample MG54 were highly oxidized (HM  $\pm 1$ ,  
391 hematite-magnetite buffer) compared to the original melt (FMQ  $\pm 1$ , fayalite-magnetite-  
392 quartz buffer) (Fialin et al., 2011). Similarly, glasses from sample MG102 also have  
393 high  $\text{Fe}^{3+}/\Sigma\text{Fe}$ , up to 0.99 in some pockets. The question of the origin of the oxidation  
394 process is discussed hereafter.

395 **Superficial oxidation of the melt.** In both samples, iron oxides were observed as  
396 fillings of cracks. We interpreted these cracks as having resulted from the release of  
397 mechanical stresses that occurred during the rapid cooling of the pocket melt (Fialin et  
398 al, 2011 for sample MG54). The width of the cracks is generally very small, which  
399 prevent accurate analysis with conventional microprobe or SEM. One of the largest (1.5  
400 - 2  $\mu\text{m}$  width) crack in MG54 was investigated in the present study with the Field-  
401 Emission Gun Scanning Electron Microscope (FEG-SEM). The crack is not chemically  
402 homogeneous, composed of two phases at least. The microanalysis of these phases gave  
403 compositions that suggest hematite for the brightest part and a Mg-rich iron oxide (e.g.  
404 magnesioferrite,  $\text{MgFe}^{3+}_2\text{O}_4$ ) for the other part (Fig. 11 and Table 3). We can reasonably  
405 speculate that these hematite and magnesioferrite phases resulted from a very late  
406 oxidation mechanism that occurred at the same time as cracks were formed in the  
407 cooling glass. The mechanism of oxidation of a volcanic glass exposed to atmospheric  
408 oxygen has been described by e.g. Cooper et al (1996), Cook and Cooper (2000), and  
409 Minitti et al. (2002). Within this mechanism, glass oxidation is likely to proceed by  
410 surface-to-bulk diffusion of holes corresponding to the change of  $\text{Fe}^{2+}$  into  $\text{Fe}^{3+}$ , instead  
411 of diffusion of oxygen species (e.g.  $\text{O}_2$ ). The hole diffusion is balanced by the migration  
412 to the free surface of network-modifying cations ( $\text{Mg}^{2+}$ ,  $\text{Ca}^{2+}$ ,  $\text{Fe}^{2+}$ ...) that form  
413 surfacial coatings of oxide species. The coprecipitation of MgO and  $\text{Fe}_2\text{O}_3$  molecules

|

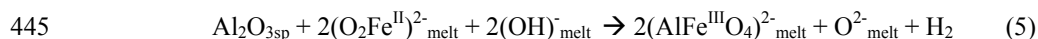
414 would have so formed magnesioferrite at the freshly formed air-crack interface.  
415 However, it must be pointed out that this mechanism only affects near surface layers  
416 (few microns) and, thus, does not involve bulk oxidation.

417 **Has spinel corrosion induced the bulk melt oxidation?** Melt oxidation is  
418 generally discussed by considering water as an oxidizing agent, although this remains  
419 highly debated (e.g. Crabbtree and Lange, 2012, and references therein; Cottrell and  
420 Kelley 2011, and references therein). The question is whether the  $\text{Fe}^{2+}$  oxidation can  
421 occur via the general reaction 4:



423 The production of  $\text{H}_2$  via the reduction of  $\text{H}_2\text{O}$  is a key phenomenon that controls  $\text{Fe}^{2+}$   
424 oxidation upon reducing conditions. The redox reaction 4 particularly applies via  
425 supercritical water/ultramafic rocks interactions in subduction zones with low oxygen  
426 fugacities under standard temperature and pressure conditions, the so-called  
427 serpentinization process (e.g. Andreani et al., 2013 and references therein). Molecular  
428 hydrogen emissions are also detected as a surface degassing species from alkali magmas  
429 (e.g. Moussallam et al., 2012; and references therein). At higher P and T conditions in  
430 the mantle,  $\text{H}_2$  may be a significant hydrous species dissolved in silicate liquids  
431 (Hirschmann et al., 2012). This means that some quantities of  $\text{Fe}^{3+}$  could be produced  
432 under high pressure as water is accommodated in silicate melt. Our present pocket melts  
433 exhibit  $f\text{O}_2$ s for their pristine compositions falling within the range for subcontinental  
434 lithospheric mantle (FMQ  $\pm 1$ ). These oxidized conditions prevent the degassing of  
435 sufficient  $\text{H}_2$  to oxidize the melt FeO at the elevated levels measured. An alternative  
436 dehydrogenation process must be thus envisioned to explain the high oxidation states of  
437 both melts.

438 In this respect, a relationship between the accommodation of  $\text{Al}_2\text{O}_{3\text{sp}}$  molecules  
439 (reactions 1 to 3) with the  $\text{Fe}^{2+}$  oxidation could be tentatively established. The major  
440 disadvantage of reaction 1 is to consume bridging oxygens to accommodate the spinel  
441 derived  $\text{Al}^{3+}$  to the melt network. Involving non-bridging oxygens would be less energy  
442 consuming as stated above for reactions 2 and 3. The concomitant accommodation of  
443  $\text{Al}^{3+}$  and  $\text{Fe}^{3+}$  as network-modifiers can be written as the following dehydrogenation  
444 reaction 5:



446 Reaction 5 hypothesizes a  $\text{Fe}^{2+}$  oxidation mechanism involving the incorporation into a  
447 melt network of alumina produced by spinel dissolution. One network modifier  $\text{Fe}^{2+}$

448 complexes with one hydroxyl pair to result in the formation of two  $\text{Al}^{3+}$ - and  $\text{Fe}^{3+}$ -  
449 bearing anionic species as well as one hydrogen molecule. Within the ionic formalism  
450 used herein to describe the melt network,  $(\text{AlFe}^{\text{III}}\text{O}_4)^{2-}$  represents two non-bridging  
451 oxygens neutralized by one  $(\text{AlFe}^{\text{III}}\text{O}_2)^{2+}$  cationic complex (Fig. 12). Reaction 5 results  
452 in a more polymerized melt (production of one bridging oxygen). Replacing reaction 1  
453 by reaction 5 in Fig. 9 would indeed illustrate the observed increase followed by the  
454 drop of the  $\text{Fe}^{3+}/\Sigma\text{Fe}$  ratios as  $\text{Al}_2\text{O}_{3\text{sp}}$  molecules were produced.

455

456

457

### IMPLICATIONS

458

459 Percolating melts through a xenolith induce or contribute to the dissolution of host  
460 minerals. Then, the released mineral-forming constituents such as  $\text{Al}_2\text{O}_3$  for spinel are  
461 accommodated to the melt network. In the first part of the present study we examined  
462 how spinel-derived  $\text{Al}_2\text{O}_3$  molecules could have been accommodated to the melt  
463 network through the investigation of fresh glass sections found in reaction zones around  
464 variably corroded spinels. At an early stage of spinel dissolution (recorded by preserved  
465 melt compositions with  $2 < \text{Mg} < 2.5$  at% in the MG54 sample),  $\text{Al}_2\text{O}_{3\text{sp}}$  molecules were  
466 presumably accommodated to the melt network through the formation of network  
467 modifying units (reaction 1). The investigation of reaction zones with highly corroded  
468 spinel (e.g. zones 1 and 2 of the MG102 sample,  $1 < \text{Mg} < 1.2$  at %), showed that the  
469 spinel dissolution proceeded till the latest stage of eruption through the dehydration  
470 reaction 3. This reaction depicts how the  $\text{Al}_2\text{O}_{3\text{sp}}$  molecules were ultimately  
471 accommodated to the melt as network-forming unit, noted  $(\text{AlO}_4/\text{K})^{4-}$ . In this case, the  
472 tetrahedra stabilizing cations  $\text{K}^+$  were extracted from the dehydrating melt.

473

474 Unlike the MG54 melt, the  $\text{Al}_2\text{O}_3$  content of the MG102 melt dropped with  
475 dropping Mg, showing that more and more  $\text{Al}_2\text{O}_{3\text{sp}}$  molecules were exsolved as  
476 dehydration (and correlative spinel corrosion) proceeded. A  $\text{Fe}^{2+}$  oxidation mechanism  
477 induced by spinel corrosion is also proposed consisting in a dehydrogenation reaction  
478 accompanied with the formation of bonded anionic complexes associating spinel-  
479 derived  $\text{Al}^{3+}$  ions and  $\text{Fe}^{3+}$  ions formed by oxidation of  $\text{Fe}^{2+}$  network modifiers.

479 This study particularly shows how a melt percolating through a mineral  
480 assemblage can accommodate chemical elements released from minerals undergoing

481

481 dissolution. This process could be related to important changes in the oxidation state of  
482 the melt.  
483

484 **APPENDIX A: PETROGRAPHIC DESCRIPTION**

485 Sample MG102 (Fig. 1) has a coarse-grained protogranular/porphyroclastic  
486 microstructure (according to the terminology of Mercier and Nicolas, 1975). It contains  
487 large orthopyroxene (up to 5.3 mm) and olivine (up to 3.3 mm) with curvilinear crystal  
488 boundaries. Thin exsolution lamellae of clinopyroxene are sometimes observed in the  
489 larger orthopyroxene, whereas undulose extinction or kink band are rarely observed in  
490 olivine. Neoblasts of olivine are similar to those of sample MG54. Clinopyroxene and  
491 spinel are smaller (usually ~ 2 mm); clinopyroxene may exhibit a spongy texture  
492 depending of its location in the thin section, and interstitial brown Cr-spinel have a  
493 vermicular shape. Spinel from zones 1 and 2 show large reaction zones compared to  
494 spinels from the other zones 3 and 4 (Fig. 1).

495 Sample MG54 (Fig. 2) has a microstructure intermediate between protogranular  
496 and porphyroclastic-tabular (Mercier and Nicolas, 1975). It is medium-grained with  
497 larger (2 - 3 mm) - sometimes kink-banded - olivine and orthopyroxene than  
498 clinopyroxene and brown Cr-spinel (1 - 2 mm). Smaller polygonal and annealed  
499 neoblasts of olivine may exhibit typical 120° triple junctions. The sample shows  
500 discontinuous alignments of Cr-spinels surrounded by reaction zones, in which  
501 pargasite occurs as a few small (100 - 150 μm) and often rounded inclusions in  
502 pyroxene (Fig. 2d).

503  
504

505 **APPENDIX B: CHEMICAL COMPOSITION OF THE PRIMARY AND SECONDARY SILICATE**  
506 **MINERALS**

507 In both samples, primary olivine, orthopyroxene and clinopyroxene (diopside) are  
508 in chemical equilibrium with high  $mg^*$  ( $mg^* = 100 * \text{molar Mg} / (\text{Mg} + \text{Fe}^{2+})$ ) of 90 - 91,  
509 although clinopyroxene may be slightly more magnesian ( $mg^*$  up to 93). They are  
510 homogeneous and show no compositional gradients whatever their location in the  
511 xenolith, next to the basanite contact or in the interior of the xenolith, and close - or not  
512 - to reaction pockets. In sample MG54, amphibole is a pargasite less magnesian ( $mg^* =$   
513 86-87) and richer in  $\text{TiO}_2$  and  $\text{Cr}_2\text{O}_3$  (~ 1.6 wt. % and 1.3 wt. %, respectively) than  
514 clinopyroxene. Primary diopside contains 0.2 - 0.6 wt. % of  $\text{TiO}_2$ , less than 1 wt.%  
515  $\text{Cr}_2\text{O}_3$  and ~ 6 wt. % of  $\text{Al}_2\text{O}_3$  in sample MG54 compared to 4 - 6 wt. % in sample  
516 MG102, and more variable (2.5 - 6 wt. %) content in the sieved clinopyroxene from the  
517 latter.

|





538  
539  
540  
541  
542  
543  
544  
545  
546  
547  
548  
549  
550  
551  
552  
553  
554  
555  
556  
557  
558  
559  
560  
561  
562  
563  
564  
565  
566  
567  
568  
569  
570  
571  
572  
573  
574  
575  
576  
577  
578  
579  
580  
581  
582  
583  
584  
585

#### REFERENCES CITED

- Andreani, M., Muñoz, M., Marcaillou, C., Delacour, A. (2013)  $\mu$ XANES study of iron redox state in serpentine during oceanic serpentinization. *Lithos*, 178, 70-83.
- Balcone-Boissard, H., Baker, D.R., Villemant, B., and Boudon, G. (2009) F and Cl diffusion in phonolitic melts: Influence of the Na/K ratio. *Chemical geology*, 263, 89-98.
- Ban, M., Witt-Eickschen, G., Klein, M., and Seck, H.A. (2005) The origin of glasses in hydrous mantle xenoliths from the West Eifel, Germany: incongruent break down of amphibole. *Contributions to Mineralogy and Petrology*, 148, 511-523.
- Bottinga, Y., and Weill, D.F. (1972) The viscosity of magmatic silicate liquids: a model for calculation. *American Journal of Science*, 272, 438-475.
- Carpenter, D.A., Edgar, A.D., and Thibault, Y. (2002) Origin of spongy textures in clinopyroxene and spinel from mantle xenoliths, Hessian depression, Germany. *Mineralogy and Petrology*, 74, 149-162.
- Coltorti, M., and Grégoire, M. (2008) Metasomatism in oceanic and continental lithospheric mantle. *Geological Society, Special Publication 293*. Eds: Coltorti, M. and Grégoire, M. 361pp.
- Coltorti, M., Beccaluva, L., Bonadiman, C., Salvini, L., and Siena, F. (2000) Glasses in mantle xenoliths as geochemical indicators of metasomatic agents. *Earth and Planetary Science Letters*, 183, 303-320.
- Cook, G.B., and Cooper, R.F. (2000) Iron concentration and the physical processes of dynamic oxidation in an alkaline earth aluminosilicate glass. *American Mineralogist*, 85, 397-406.
- Cooper, R.F., Fanselow, J.B., and Poker, D.B. (1996) The mechanism of oxidation of a basaltic glass: Chemical diffusion of network-modifying cations. *Geochimica et Cosmochimica Acta*, 60, 3253-3265.
- Cottrell, E., and Kelley, K.A. (2011) The oxidation state of Fe in MORB glasses and the oxygen fugacity of the upper mantle. *Earth and Planetary Science Letters*, 305, 270-282.
- Crabtree, S.M., and Lange, R.A. (2012) An evaluation of the effect of degassing on the oxidation state of hydrous andesite and dacite magmas: a comparison of pre- and post-eruptive Fe<sup>2+</sup> concentrations. *Contributions to Mineralogy and Petrology*, 163, 209-224.
- Downes, H. and Dupuy, C. (1987) Textural, isotopic and REE variations in spinel peridotite xenoliths, Massif Central, France. *Earth and Planetary Science Letters*, 82, 121-135.

- 586 Downes, H., Reichow, M.K., Mason, P.R.D., Beard, A.D., and Thirlwall, M.F. (2003)  
587 Mantle domains in the lithosphere beneath the French Massif Central: trace element and  
588 isotopic evidence from mantle clinopyroxenes. *Chemical Geology*, 200, 71-87.  
589
- 590 | Draper, D.S., and Green, T.H. (1999) P - T phase relations of silicic, alkaline, aluminous  
591 liquids: new results and applications to mantle melting and metasomatism. *Earth and*  
592 *Planetary Science Letters*, 170, 255-268.  
593
- 594 Féménias, O., Coussaert, N., Berger, J., Mercier, J.-C., and Demaiffe, D. (2004)  
595 Metasomatism and melting history of a Variscan lithospheric mantle domain: evidence  
596 from the Puy Beaunit xenoliths (French Massif Central). *Contributions to Mineralogy*  
597 *and Petrology*, 148, 13-28.  
598
- 599 Fialin, M., Wagner, C., Métrich, N., Humler, E., Galois, L. and Bézou, A. (2001)  
600  $Fe^{3+}/\Sigma Fe$  vs.  $Fe-L\alpha$  peak energy for minerals and glasses: recent advances with the  
601 electron microprobe. *American Mineralogist*, 86, 456-465.  
602
- 603 Fialin, M., Bézou, A., Wagner, C., Magnien, V. and Humler, E. (2004) Quantitative  
604 electron microprobe analysis of  $Fe^{3+}/\Sigma Fe$ : Basic concepts and experimental  
605 protocol for glasses. *American Mineralogist*, 89, 654-662.  
606
- 607 Fialin, M., Wagner, C., and Pascal, M.-L. (2011) Iron speciation using electron microprobe  
608 techniques: application to glassy melt pockets within a spinel lherzolite xenolith.  
609 *Mineralogical Magazine*, 75, 349-364.  
610
- 611 Granet, M., Wilson, M., and Achauer, U. (1995) Imaging a mantle plume beneath the  
612 French Massif Central. *Earth and Planetary Science Letters*, 136, 281-296.  
613
- 614 Granet, M., Judenherc, S. and Souriau, A. (2000) Des images du système lithosphere-  
615 asthénosphère sous la France et leurs implications géodynamiques : l'apport de la  
616 tomographie télésismique et de l'anisotropie sismique. *Bulletin de la Société*  
617 *Géologique de France*, 171, 149-167.  
618
- 619 Hirschmann, M.M., Withers, A.C., Ardia, P., and Foley, N.T. (2012) Solubility of  
620 molecular hydrogen in silicate melts and consequences for volatile evolution of  
621 terrestrial planets. *Earth and Planetary Science Letters*, 345-348, 38-48.  
622
- 623 Hoernle, K., Zhang, Y.S., and Graham, D. (1995) Seismic and geochemical evidence for  
624 large-scale mantle upwelling beneath the eastern Atlantic and western and central  
625 Europe. *Nature*, 374, 34-38.  
626
- 627 Ismail, M., Delpéch, G., Cottin, J.-Y., Grégoire, M., Moine, B.N., and Bilal, A. (2008)  
628 Petrological and geochemical constraints on the composition of the lithospheric mantle  
629 beneath the Syrian rift, northern part of the Arabian plate. In: *Metasomatism in oceanic*  
630 *and continental lithospheric mantle*. Eds: Coltorti, M. and Grégoire, M. Geological  
631 Society, London, Special Publication, 293, 223-251.  
632
- 633 Jardin, L. (1973) Les enclaves basiques et ultrabasiques dans les basaltes alcalins de la  
634 Chaîne du Devès (Haute Loire). Thèse de Doctorat de 3<sup>ème</sup> cycle, Université de Lyon,  
635 pp. 119.

- 636  
637 Kushihiro, I. (1975) On the nature of silicate melt and its significance in magma genesis:  
638 regularities in the shift of the liquidus boundaries involving olivine, pyroxene, and silica  
639 minerals. *American Journal of Science*, 275, 411-431.  
640  
641 Le Bas, M.J., Le Maitre, R.W., Streckeisen, A., and Zanettin, B.A. (1986) Chemical  
642 classification of volcanic rocks based on the total alkali – silica diagram. *Journal of*  
643 *Petrology*, 27, 745-750.  
644  
645 Lenoir, X., Garrido, C.J., Bodinier, J.-L., and Dautria, J.-M. (2000) Contrasting  
646 lithospheric mantle domains beneath the Massif Central (France) revealed by  
647 geochemistry of peridotite xenoliths. *Earth and Planetary Science Letters*, 181, 359-375.  
648  
649 Lesne, P., Scaillet, B., Pichavant, M., Iacono-Marziano, G., and Beny, J.-M. (2011). The  
650 H<sub>2</sub>O solubility of alkali basaltic melts: an experimental study. *Contributions to*  
651 *Mineralogy and Petrology*, 162, 133-151.  
652  
653 Lo Cascio, M., Liang, Y., Shimizu, N., and Hess, P.C. (2008) An experimental study of the  
654 grain-scale processes of peridotite melting: implications for major and trace element  
655 distribution during equilibrium and disequilibrium melting. *Contributions to Mineralogy*  
656 *and Petrology*, 156, 87-102.  
657  
658 Maaloe, S., and Printzlau, I. (1979) Natural partial melting of spinel lherzolite. *Journal of*  
659 *Petrology*, 20, 727-741.  
660  
661 Maury, R., and Varet, J. (1980) Le volcanisme tertiaire et quaternaire. In : Autran, A. and  
662 Dercourt, J. (Coord.), Colloque C7, Géologie de la France, Mémoire du BRGM, 107,  
663 138-159.  
664  
665 Mercier, J.C., and Nicolas, A. (1975) Textures and fabrics of upper-mantle peridotites as  
666 illustrated by xenoliths from basalts. *Journal of Petrology*, 16, 454-487.  
667  
668 Mergoïl, J., and Boivin, P. (1993) Le Velay. Son volcanisme et les formations associées.  
669 *Géologie de la France*, 3, 3-96.  
670  
671 Minitti, M.E., Mustard, J.F., and Rutherford, J.R. (2002) Effects of glass content and  
672 oxidation on the spectra of SNC-like basalts: Application to Mars remote sensing.  
673 *Journal of Geophysical Research*, 107, E5, 5030,6-1, 6-11.  
674  
675 Moussalam, Y., Oppenheimer, C., Aiuppa, A., Giudice, G., Moussalam, M., and Kyle, P.,  
676 (2012) Hydrogen emissions from Erebus volcano, Antarctica. *Bulletin of Volcanology*,  
677 74-9, 2109-2120.  
678  
679 Mysen B.O., and Acton, M. (1999) Water in H<sub>2</sub>O-saturated magma–fluid systems;  
680 solubility behavior in K<sub>2</sub>O-Al<sub>2</sub>O<sub>3</sub>-SiO<sub>2</sub>-H<sub>2</sub>O to 2.0 GPa and 1300°C. *Geochimica et*  
681 *Cosmochimica Acta*, 63, 3799-3815.  
682  
683 Perinelli, C., Orlando, A., Conte, A.M., Armienti, P., Borrini, D., Faccini, F., and Misiti,  
684 V. (2008) Metasomatism induced by alkali magma in the upper mantle of northern  
685 Victoria Land (Antarctica): an experimental approach. In: *Metasomatism in oceanic and*

- 686 continental lithospheric mantle. Eds: Coltorti, M. and Grégoire, M. Geological Society,  
687 London, Special Publication, 293, 279-302.  
688
- 689 Pichavant, M., Holtz, and F., McMillan, P.F. (1992) Phase relations and compositional  
690 dependence of H<sub>2</sub>O solubility in quartz-feldspar melts. *Chemical Geology*, 96, 303-319.  
691
- 692 Shaw, C.S.J. (1999) Dissolution of orthopyroxene in basanitic magma between 0.1 and 2  
693 GPa: further implications for the origin of Si-rich alkaline glass inclusions in mantle  
694 xenoliths. *Contributions to Mineralogy and Petrology*, 135, 114-132.  
695
- 696 Shaw, C.S.J. (2009) textural development of amphibole during breakdown reactions in a  
697 synthetic peridotite. *Lithos*, 110, 215-228.  
698
- 699 Shaw, C.S.J., and Dingwell, D.B. (2008) Experimental peridotite-melt reaction at one  
700 atmosphere: a textural and chemical study. *Contributions to Mineralogy and Petrology*,  
701 155, 199-214.  
702
- 703 Shaw, C.S.J., and Klügel, A. (2002) The pressure and temperature conditions and timing of  
704 glass formation in mantle-derived xenoliths from Baarley, West Eifel, Germany: the  
705 case for amphibole breakdown, lava infiltration and mineral-melt reaction. *Mineralogy  
706 and Petrology*, 74, 169-187.  
707
- 708 Shaw, C.S.J., Thibault, Y., Edgar, A.D., and Lloyd, F.E. (1998) Mechanisms of  
709 orthopyroxenes dissolution in silica-undersaturated melts at one atmosphere and  
710 implications for the origin of silica-rich glass in mantle xenoliths. *Contributions to  
711 Mineralogy and Petrology*, 132, 354-370.  
712
- 713 Shaw, C.S.J., Heidelberg, F., and Dingwell, D.B. (2006) The origin of reaction textures in  
714 mantle peridotite xenoliths from Sal Island, Cape Verde: the case for “metasomatism”  
715 by the host lava. *Contributions to Mineralogy and Petrology*, 151, 681-697.  
716
- 717 Su, B.-X., Zhang, H.-F., Asamoah Saki, P., Yang, Y.-H., Ying, J.-F., Tang, Y.J., Qin, K.-  
718 Z., Xiao, Y., Zhao, X.-M., Mao, Q., and Ma, Y.-G. (2011) The origin of spongy texture  
719 in minerals of mantle xenoliths from the Western Qinling, central China. *Contributions  
720 to Mineralogy and Petrology*, 615, 465-482.  
721
- 722 Touron, S., Renac, C., O'Reilly, S.Y, Cottin, J.-Y., and Griffin, W.L. (2008)  
723 Characterization of the metasomatic agent in mantle xenoliths from Devès (France)  
724 using coupled in situ trace-element and O, Sr and Nd isotopic compositions. In:  
725 *Metasomatism in oceanic and continental lithospheric mantle*. Eds: Coltorti, M. and  
726 Grégoire, M. Geological Society, London, Special Publication, 293, 177-196.  
727
- 728 Vanucci, R., Ottolini, L., Bottazi, P., Downes, H., and Dupuy, C. (1994) INAA, IDMS and  
729 SIMS comparative REE investigations of clinopyroxenes from mantle xenoliths with  
730 different textures. *Chemical Geology*, 118, 85-108.  
731
- 732 Wagner C., and Deloule, E. (2007) Behaviour of Li and its isotopes during metasomatism  
733 of French Massif Central lherzolites. *Geochimica et Cosmochimica Acta*, 71, 4279-  
734 4296.  
735

- 736 Wang, Y., Han, B., Griffin, W.L., Zhang, L., and Shu, G. (2012) Post-entrainment mineral-  
737 magma interaction in mantle xenoliths from Inner Mongolia, western North China  
738 Craton. *Journal of Earth Science*, 23, 64-76.  
739
- 740 Wilson, M. and Downes, H. (1991) Tertiary-Quaternary extension-related magmatism in  
741 western and central Europe. *Journal of Petrology*, 32, 811-849.  
742
- 743 Xu, Y.G., Menziers, M.A., Bodinier, J.-L., Bedini, R.M., Vroon, P., and Mercier, J.-C.  
744 (1998) Melt percolation and reaction atop a plume: evidence from the poikiloblastic  
745 peridotite xenoliths from Borée (Massif Central, France). *Contributions to Mineralogy  
746 and Petrology*, 132, 65-84.  
747
- 748 Zangana, N.A., Downes, H., Thirlwall, M.F., and Hegner, E. (1997) Relationship between  
749 deformation, equilibration temperature, REE and radiogenic isotopes in mantle  
750 xenoliths (Ray Pic, Massif Central, France): an example of plume-lithosphere  
751 interaction ? *Contributions to Mineralogy and Petrology*, 127, 187-203.  
752

753  
754

#### TABLE CAPTIONS

755

**Table 1:** Spinel compositions (average of 10 spot analyses).

756

**Table 2:** Glass compositions.

757

**Table 3:** Energy dispersive analysis of both oxide phases depicted in figure 11.

758

759

760

761

#### FIGURE CAPTIONS

762

763

**Figure 1.** Sample MG102. General view (a) and detailed boxes (b to g). (b) Lherzolite - host basanite contact showing sieve-textured clinopyroxene (cpx) and glassy percolation paths. (c) Reaction zone developed around spinel in zone 2. Cpx, orthopyroxene (opx) and olivine (ol) refer to primary minerals. Note that cpx is sieve-textured. Details of the reaction zone are given in figure 6. (d) Destabilized opx at the contact with the host vesicular basanite. (e) Reaction zone developed around spinel in zone 1. (f) Poorly corroded spinel 4.7 in reaction zone 4 (details in figure 4). (g) Uncorroded spinel from zone 3. All views in transmitted light.

770

771

772

**Figure 2.** Sample MG54. (a) General view (in transmitted light) and detailed boxes (b to d). (b) and (c) Al<sub>2</sub>O<sub>3</sub> (b) and CaO (c) elemental maps showing the glassy framework of the reaction zones developed in spinel band. (d) Detail of the reaction zone developed around spinel (sp, in black) showing glass (gl) and relict amphibole (amp) in (cpx).

776

777

778

**Figure 3.** Reaction zone developed around spinel in sample MG54. (a) General view (BSE image). (b) Detail boxed in (a). (c-f) Elemental maps. (c) Al<sub>2</sub>O<sub>3</sub>; orange: sp, blue-green: glass. (d) MgO; orange: ol, green: opx, light blue: sp, blue: cpx. (e) Na<sub>2</sub>O+K<sub>2</sub>O; white: gl, blue: cpx. (f) CaO; orange: cpx; dark blue: gl. Abbreviations as in figures 1 and 2.

782

783

784

**Figure 4.** Reaction zone developed around spinel in zone 4.7 in sample MG102. Abbreviations as in figures 1 and 2.

785

786

787 **Figure 5.** Reaction zone developed around spinel in zone 1 of sample MG102. (a)  
788 General view (BSE image). (b) Detail boxed in (a). The red arrows indicate corrosion  
789 features of the primary sp core. (c-f) Elemental maps. (c) Al<sub>2</sub>O<sub>3</sub>; white: primary sp,  
790 green: gl, mixed white-green-red: corona of secondary sp around the central primary sp.  
791 (d) MgO; orange: ol, green: opx, light blue: sp, dark blue: cpx. (e) Na<sub>2</sub>O+K<sub>2</sub>O; white:  
792 gl, blue: cpx. (f) CaO; orange: cpx, dark blue: gl. Abbreviations as in figures 1 and 2.

793

794 **Figure 6.** Reaction zone developed around spinel in zone 2 of sample MG102. (a)  
795 General view (BSE image). (b-e) Elemental maps. (b) Al<sub>2</sub>O<sub>3</sub>; white-green-red: gl  
796 network. (c) Na<sub>2</sub>O+K<sub>2</sub>O; white: gl, blue: cpx. (d) MgO; orange: ol, green: opx, blue: sp,  
797 turquoise: cpx. (e) CaO; white: cpx, green: gl. Abbreviations as in figures 1 and 2.

798

799 **Figure 7.** Range of glass compositions from samples MG54 (blue diamond) and  
800 MG102 (red square) compared to host magmatic rocks of Mont Gros (black triangles;  
801 data from Jardin, 1973) plotted in the total alkali versus silica diagram after Le Bas et  
802 al. (1986).

803

804 **Figure 8.** Variations of glass compositions versus Mg expressed in atom per cent  
805 (at %) for samples MG54 (open circles) and MG102 (filled circles). Large filled circles  
806 correspond to glass compositions from MG102 reaction zones 1 and 2, which exhibit  
807 highly corroded spinels. The Al vs. Mg trend for MG54 is reinforced by the least  
808 squares fitted second order polynom (full line).

809

810 **Figure 9.** Schema of the evolution of K and Al vs. Mg for both MG54 and  
811 MG102 melts. Red lines: observed trends for MG54. Blue lines: observed trends for  
812 MG102. Note that, in accordance with figure 8 for MG102, the blue line for K must be  
813 shifted down and that for Al must be shifted up (as less K and more Al relative to MG54  
814 were present prior to reaction 2). See text for explanation.

815

816 **Figure 10.** K, Ca and Al variations (expressed in at %) versus Mg in glasses from  
817 MG102.

818

819 **Figure 11.** BSE images of a crack within sp in sample MG54 (a) filled with  
820 hematite in white and magnesioferrite in grey (b).

|



821

822

823

824

825

826

827

**Figure 12.** Schematics showing how a  $\text{Fe}^{2+}$  network modifier, represented here as neutralizing two non-bridging oxygens (left), can be oxidized through the formation of the bonded compound cation depicted in the dehydrogenation reaction 5 (right). Numbers refer to the number of electrons transferred from cations to oxygens.

|

25

828  
 829  
 830

**Table 1:** Spinel compositions (average of 10 spot analyses).

	MG54				MG102						dl <sup>a</sup> (ppm)
	primary		secondary		primary		secondary				
	range		range		zones 1-4	range	zones 3,4	range	zones 1,2	range	
SiO <sub>2</sub>	0.07	<0.08	0.12	<0.13	0.02	<0.08	0.32	<0.35	0.09	<0.23	203
TiO <sub>2</sub>	0.07	0.01-0.10	0.62	0.35-0.83	0.01	<0.02	0.09	0.05-0.16	0.31	0.11-0.52	221
Al <sub>2</sub> O <sub>3</sub>	52.05	50.30-53.01	43.84	43.64-51.01	55.37	54.35-56.91	50.71	49.53-51.95	27.58	19.79-47.89	175
Cr <sub>2</sub> O <sub>3</sub>	15.55	13.93-16.46	24.47	17.29-25.25	11.61	11.36-12.30	16.53	14.83-18.02	38.77	26.87-50.05	285
FeO	11.88	10.82-13.69	9.32	6.73-11.79	12.55	11.37-13.12	11.31	10.49-11.72	13.92	10.54-18.80	507
MnO	0.12	0.06-0.16	0.12	0.06-0.15	0.08	0.03-0.15	19.61	0.12-0.19	0.10	0.08-0.19	395
MgO	20.17	18.72-20.53	20.81	19.00-23.15	19.20	18.10-19.78	0.16	18.79-19.83	16.49	13.02-20.13	118
NiO	na	-	na	-	0.44	0.39-0.64	0.24	0.21-0.35	0.19	0.04-0.41	400
Total	99.91		99.31		99.27		98.98		97.45		
Si	0.002		0.003		0.000		0.008		0.003		
Ti	0.001		0.013		0.000		0.002		0.007		
Al	1.616		1.402		1.716		1.594		0.976		
Cr	0.324		0.525		0.241		0.349		0.920		
Fe	0.262		0.211		0.276		0.252		0.350		
Mn	0.003		0.003		0.002		0.786		0.002		
Mg	0.792		0.842		0.752		0.004		0.738		
Ni					0.012		0.005		0.006		
Fe <sup>3+</sup>	0.05		0.04		0.04		0.04		0.08		
Fe <sup>2+</sup>	0.21		0.17		0.23		0.22		0.27		
cr*	16.2	14.9-17.5	26.7	18.2-27.2	12.1	11.7-12.9	17.6	15.8-19.3	46.5	21.3-63.9	
Fe <sup>3+</sup> /ΣFe	0.20		0.20		0.15		0.14		0.24		

Note: Mineral formulae were calculated using normalization on 3 cations. n.a. = not analyzed; cr\* = 100\*(Cr/(Cr+Al+Fe<sup>2+</sup>)).  
<sup>a</sup>For each elements, the detection level (dl) represents an average value calculated from the 5 analyses.

831  
 832  
 833  
 834  
 835  
 836

837

TABLE 2. Glass compositions.

(wt%)	MG54 (A1)	MG54 (C1-1)	MG54 (C1-2)	MG54 (C2-1)	MG54 (C2-2)	MG54 (D1-2)	MG54 (D1-7)	MG54 (D1-8)	MG54 (D2-1)	MG54 (D2-2)	e.s.d. (2σ)
SiO <sub>2</sub>	56.91	54.94	55.36	55.38	54.75	54.74	55.00	54.97	55.60	55.16	0.83
TiO <sub>2</sub>	0.83	1.28	1.23	1.35	1.29	1.73	1.65	1.67	1.90	2.04	0.31
Al <sub>2</sub> O <sub>3</sub>	19.12	18.78	18.64	19.19	19.13	19.20	18.96	19.11	19.50	19.55	0.36
Cr <sub>2</sub> O <sub>3</sub>	0.07	0.22	0.11	0.04	0.02	0.06	0.04	0.07	0.17	0.22	0.1
FeO <sub>T</sub>	3.15	3.78	3.73	3.49	3.40	3.52	3.43	3.44	3.46	3.73	0.3
MnO	0.06	0.08	0.11	0.09	0.07	0.09	0.09	0.10	0.08	0.09	0.05
MgO	3.90	4.67	4.66	4.15	3.92	4.21	4.41	4.31	4.10	4.34	0.47
CaO	8.02	8.69	8.13	8.40	8.49	8.55	8.28	8.28	8.79	8.96	0.83
Na <sub>2</sub> O	4.51	3.56	4.16	4.32	4.98	4.53	4.90	4.90	3.22	3.08	0.92
K <sub>2</sub> O	2.31	1.81	1.87	1.94	1.95	1.79	1.84	1.84	1.72	1.74	0.21
P <sub>2</sub> O <sub>5</sub>	0.29	1.40	1.46	0.73	0.71	0.45	0.44	0.45	0.27	0.31	0.34
Cl	0.07	0.11	0.10	0.09	0.09	0.07	0.07	0.07	0.07	0.08	0.02
F	0.13	0.15	0.13	0.08	0.06	0.09	0.09	0.11	0.16	0.14	0.07
Total	99.38	99.47	99.71	99.25	98.87	99.03	99.20	99.32	99.03	99.42	
Fe <sup>3+</sup> /ΣFe	0.65	0.75	0.69	0.68	0.66	0.63	0.68	0.72	0.62	0.65	
FeO	1.10	0.95	1.16	1.12	1.15	1.30	1.10	1.00	1.31	1.31	
Fe <sub>2</sub> O <sub>3</sub>	2.28	3.15	2.86	2.64	2.49	2.47	2.60	2.72	2.38	2.70	
Norm CIPW											
Qz	2.4	6.4	4.6	2.8		0.8			7.6	7.2	
Or	13.7	10.7	11.1	11.5	11.3	10.6	10.9	10.9	10.2	10.3	
Lc											
Ab	38.1	30.1	35.1	36.5	42.1	38.3	41.4	41.4	27.2	26.0	
Ne											
An	25.1	29.9	26.6	27.2	24.2	26.7	24.3	24.7	33.6	34.3	
Cor											
Aeg											
Di	10.0	3.0	3.3	7.6	10.4	9.5	10.0	9.3	5.4	5.0	
Wo		0.2				0.3	0.5	0.6	0.5	0.7	
Hy	5.1	10.3	10.1	6.9	2.7	6.1	3.6	3.5	7.7	8.5	
Ol					1.6		2.0	2.1			
Mt	1.3		0.5		0.2						
Ht	1.4	3.2	2.5	2.6	2.4	2.5	2.6	2.7	2.4	2.7	
Ilm	1.6	2.2	2.3	2.6	2.5	2.9	2.5	2.3	2.9	3.0	
Ap	0.7	3.2	3.4	1.7	1.6	1.0	1.0	1.0	0.6	0.7	
Sp		0.3				0.5	0.8	1.1	0.9	1.2	
Pv											
Total	99.4	99.5	99.5	99.4	99.0	99.2	99.6	99.6	99.0	99.6	

Note: \* For each elements, the detection level (dl) represents an average value calculated from the 15 analyses listed; e.s.d. = Estimated standard deviation at 2σ.

838

839

840

841

842

843

844

845

846

847

848

849

850

TABLE 2. (continued)

(wt%)	MG102 (zone 1)	MG102 (zone 2)	MG102 (zone 3)	MG102 z 4-2,4-3,4	MG102 (zone 4-7)	e.s.d. (2 $\sigma$ )	di <sup>§</sup> (ppm)
SiO <sub>2</sub>	59.45	61.41	58.16	57.66	55.10	0.84	185
TiO <sub>2</sub>	0.32	0.48	0.32	0.35	0.40	0.29	193
Al <sub>2</sub> O <sub>3</sub>	19.58	18.51	20.67	20.59	21.18	0.36	156
Cr <sub>2</sub> O <sub>3</sub>	0.06	0.12	0.20	0.13	0.15	0.10	256
FeO <sub>T</sub>	2.59	2.71	3.18	3.30	3.75	0.28	492
MnO	0.01	0.12	0.06	0.06	0.06	0.05	376
MgO	2.30	2.09	3.57	3.68	4.01	0.39	93
CaO	2.83	2.53	6.48	6.95	8.31	0.73	271
Na <sub>2</sub> O	7.55	7.02	6.37	5.96	5.41	1.01	480
K <sub>2</sub> O	4.66	5.07	0.97	0.83	0.52	0.47	186
P <sub>2</sub> O <sub>5</sub>	0.06	0.07	0.07	0.09	0.10	0.11	116
Cl	0.09	0.07	0.18	0.21	0.24	0.02	145
F	0.05	0.07	0.03	0.03	0.02	0.06	575
Total	99.59	100.27	100.26	99.83	99.25		
Fe <sup>3+</sup> / $\Sigma$ Fe	0.57	0.63	0.74	0.88	0.99		
FeO	1.12	1.00	0.83	0.40	0.04		
Fe <sub>2</sub> O <sub>3</sub>	1.64	1.90	2.62	3.23	4.13		
Norm CIPW							
Qz				1.2			
Or	27.6	30.0	5.7	4.9	3.1		
Lc							
Ab	44.1	49.1	53.8	50.4	45.7		
Ne	10.7	5.5					
An	5.7	4.0	24.9	26.9	31.7		
Cor							
Aeg							
Di	6.2	6.3	5.3	5.4	6.0		
Wo					0.4		
Hy			6.1	6.7	6.6		
Ol	2.2	1.6	0.3		0.4		
Mt	2.4	2.2	1.9	0.5			
Ht		0.4	1.3	2.9	4.1		
Ilm	0.6	0.9	0.6	0.7	0.2		
Ap	0.1	0.2	0.2	0.2	0.2		
Sp					0.7		
Pv							
Total	99.6	100.2	100.1	99.8	99.1		

851  
 852  
 853  
 854  
 855  
 856  
 857  
 858  
 859  
 860  
 861

862  
863  
864  
865

**Table 3:** Energy dispersive analysis of both oxide phases depicted in figure 11.

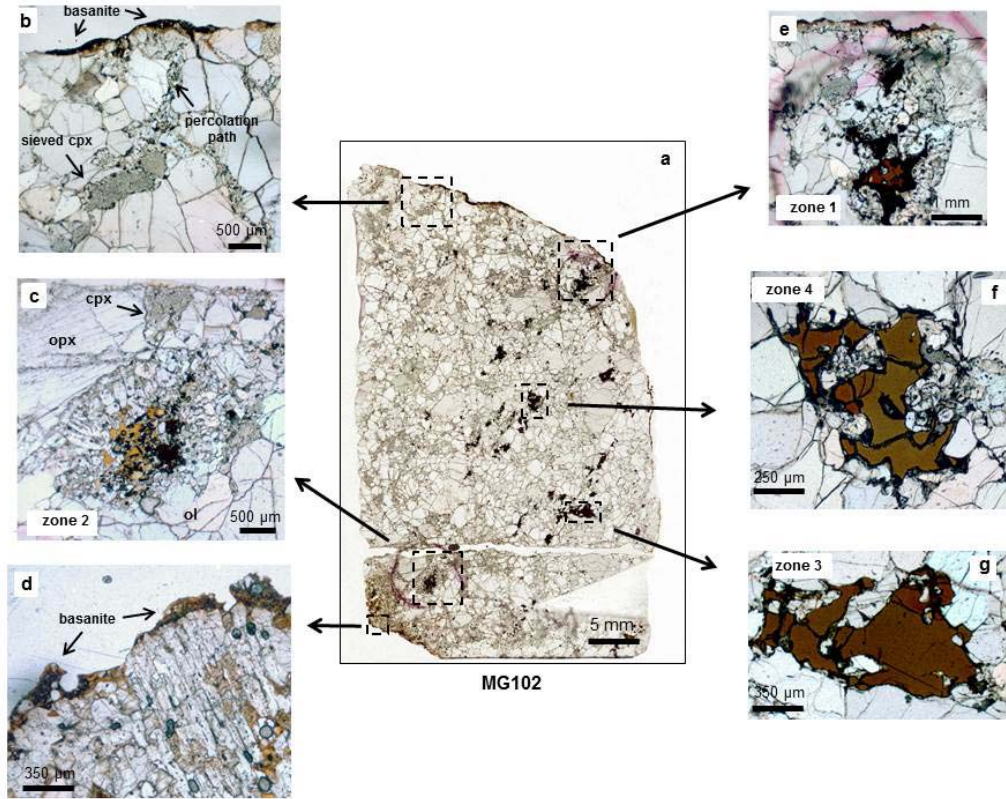
	<b>hematite</b>		<b>magnesioferrite</b>	
(wt%)		±		±
SiO <sub>2</sub>	1.31	0.45	2.42	0.47
Al <sub>2</sub> O <sub>3</sub>	1.41	0.39	1.44	0.39
MgO	1.09	0.38	15.4	0.78
Cr <sub>2</sub> O <sub>3</sub>	1.77	0.41	1.43	0.42
Fe <sub>2</sub> O <sub>3</sub>	95.04	1.08	79.44	1.04
Total	100.61		100.03	
(at%)				
Si	0.68		1.16	
Al	0.86		0.81	
Mg	0.84		10.96	
Cr	0.73		0.54	
Fe	37.17		28.51	
O	60.33		58.06	

*Note:* The error is estimated at 2σ; at% = atom per cent.

866  
867  
868  
869  
870

871  
872  
873

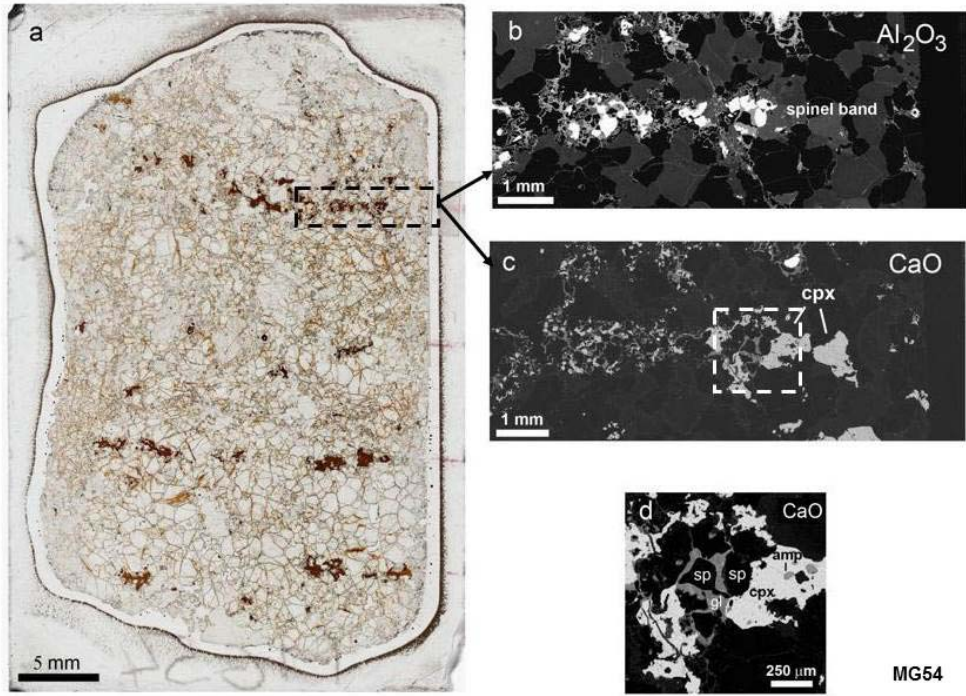
**Figure 1.**



874  
875  
876

877  
878  
879  
880

**Figure 2.**



881  
882  
883

884  
885  
886  
887  
888  
889  
890

Figure 3.

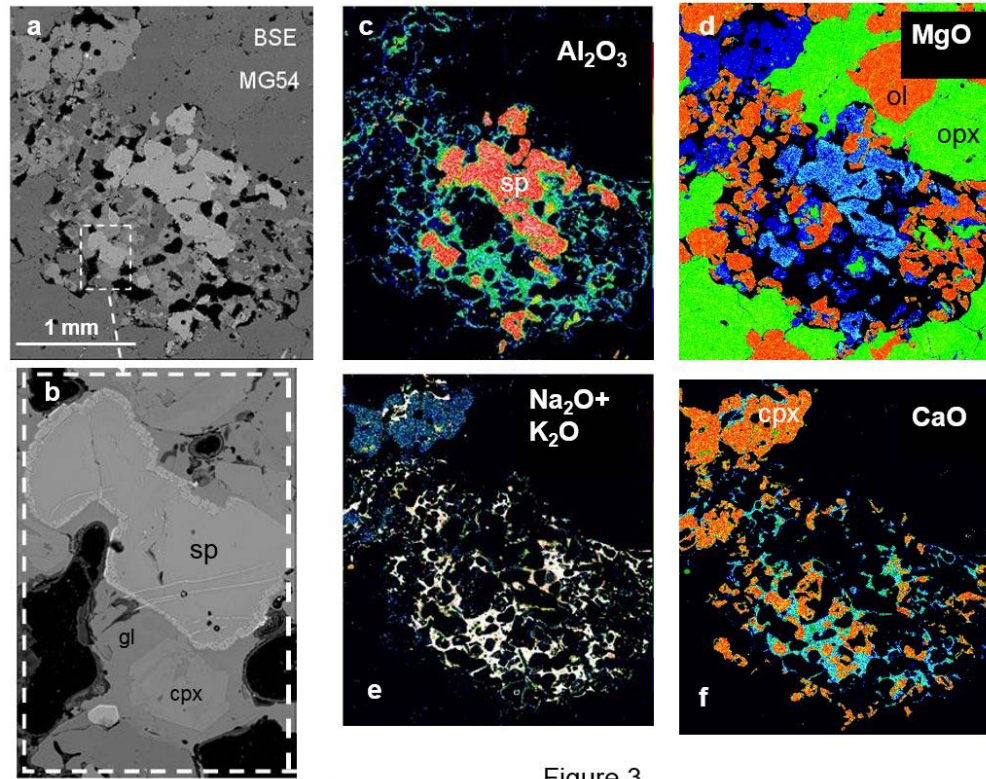


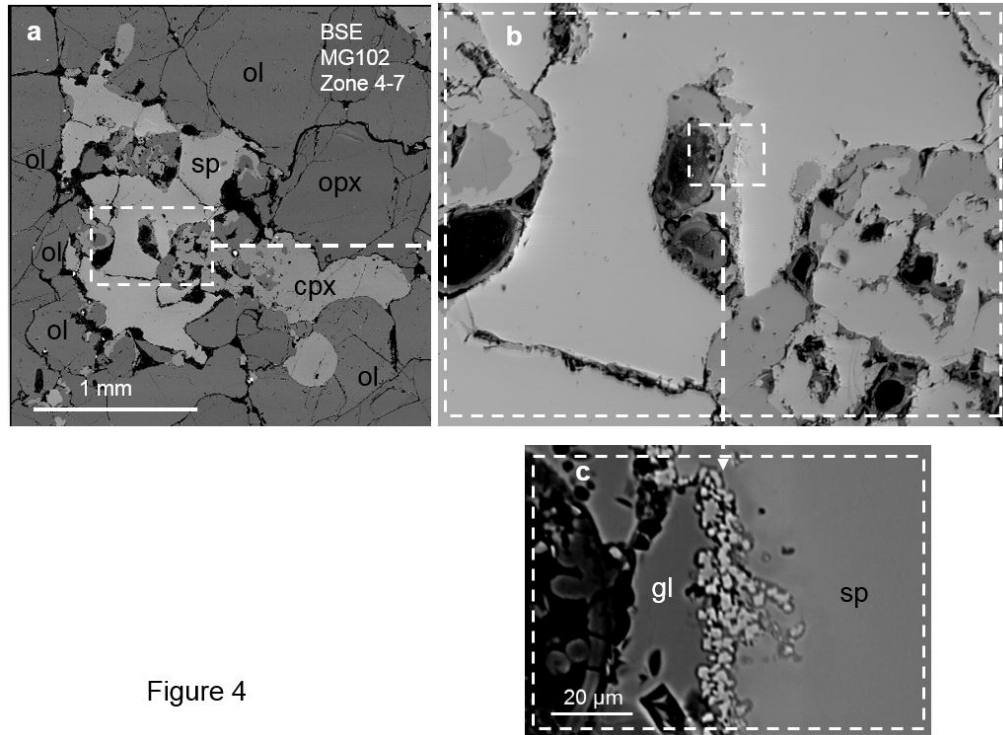
Figure 3

891  
892  
893  
894



895  
896  
897  
898

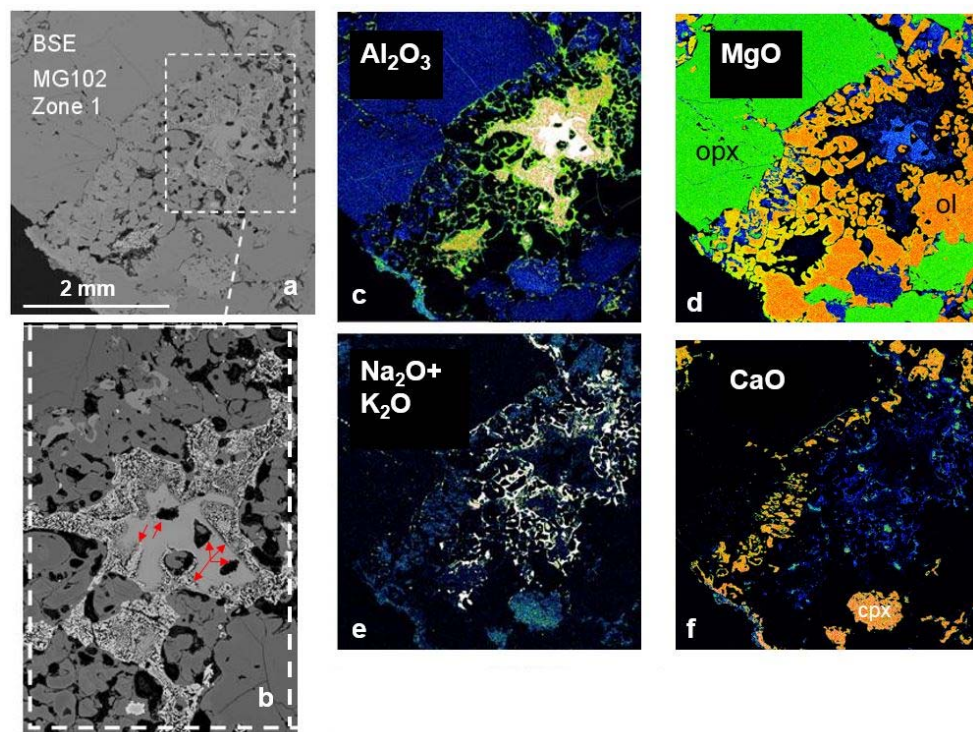
**Figure 4.**



899  
900  
901  
902  
903  
904  
905  
906  
907  
908  
909  
910  
911  
912  
913  
914  
915  
916  
917

918  
919

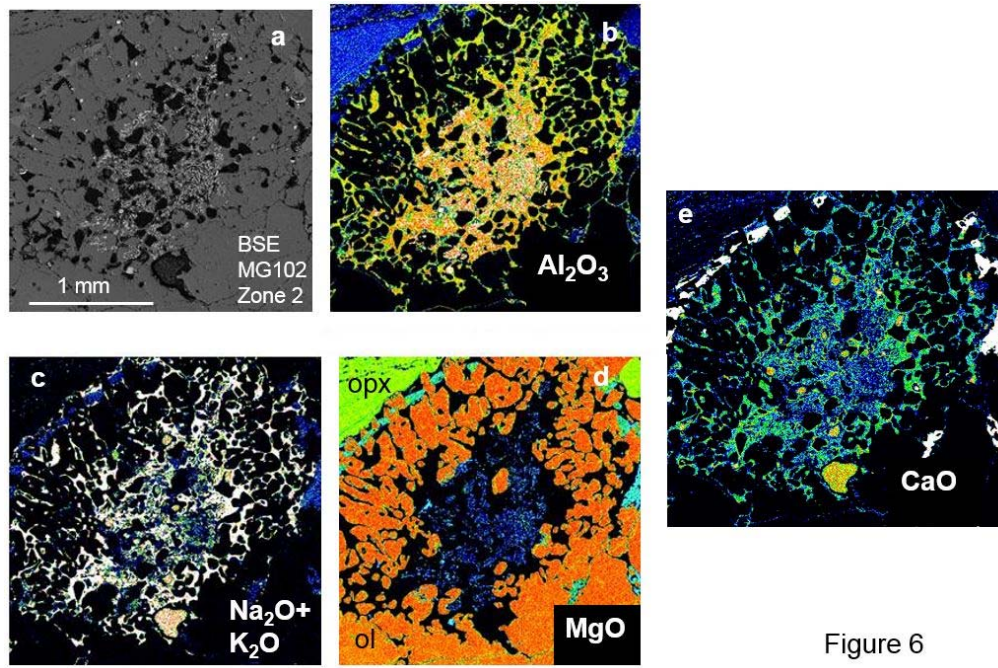
**Figure 5.**



920  
921  
922

Figure 5

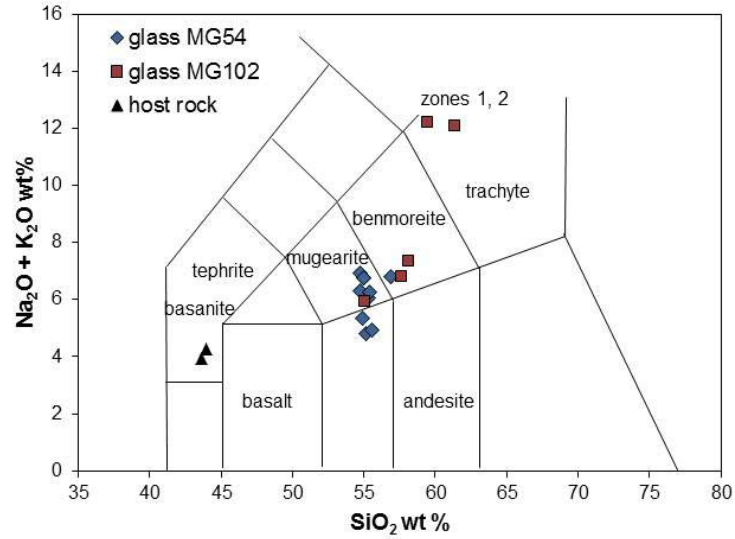
923 **Figure 6.**  
924  
925



926  
927  
928  
929

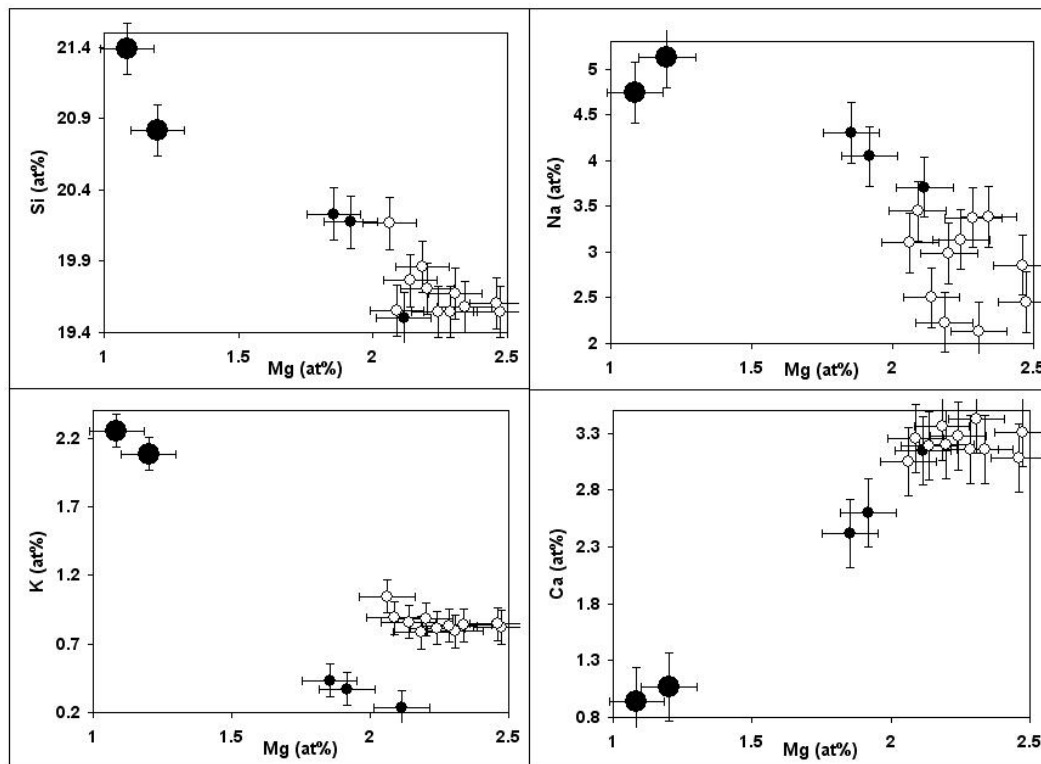
Figure 6

930  
931 **Figure 7.**  
932  
933



934  
935

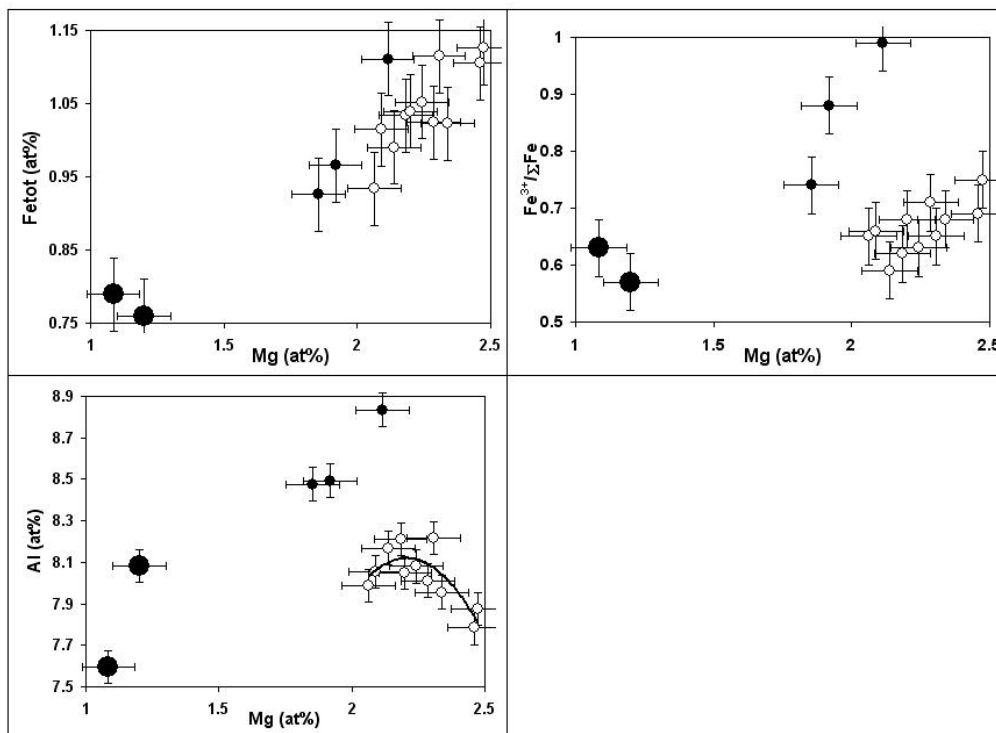
936 **Figure 8.**  
937  
938



939  
940  
941

942  
943

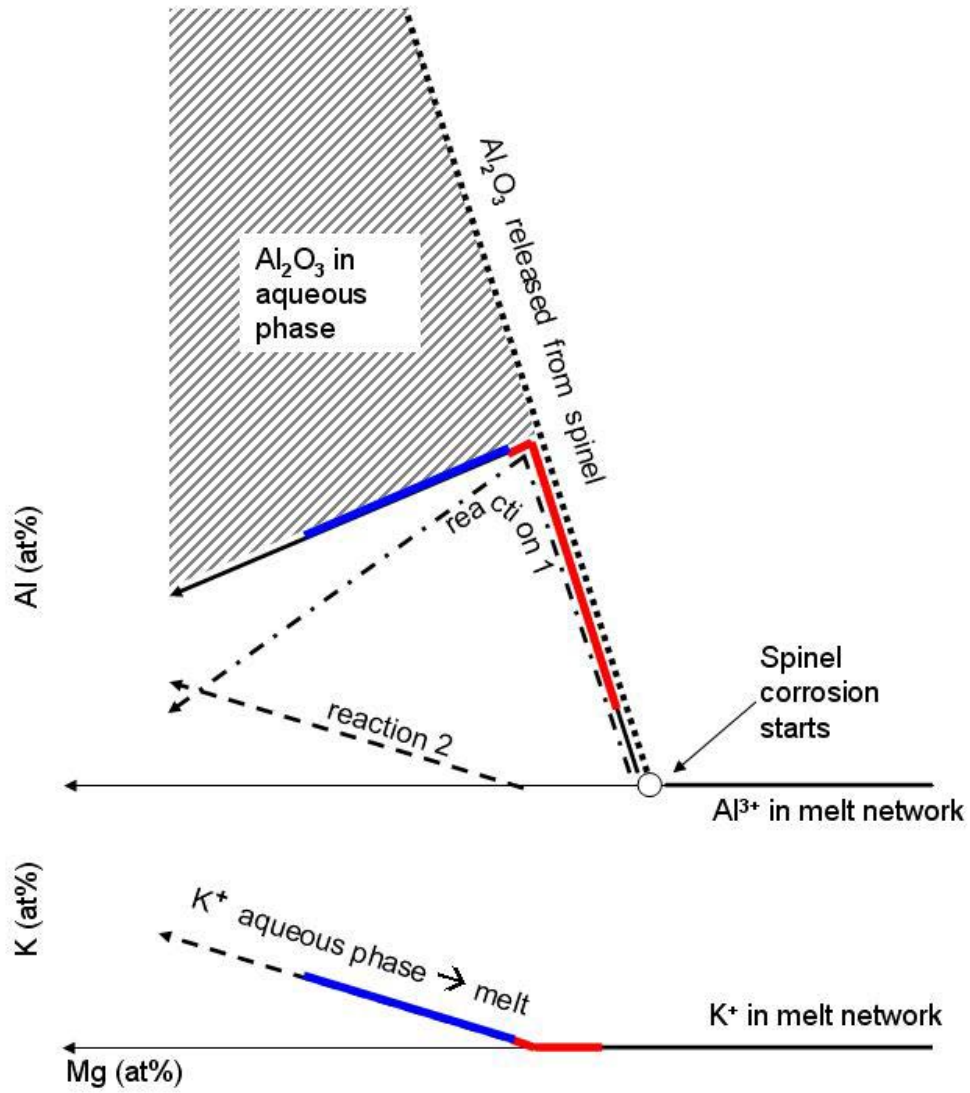
**Figure 8.** continued



944  
945  
946

947  
948  
949

Figure 9.

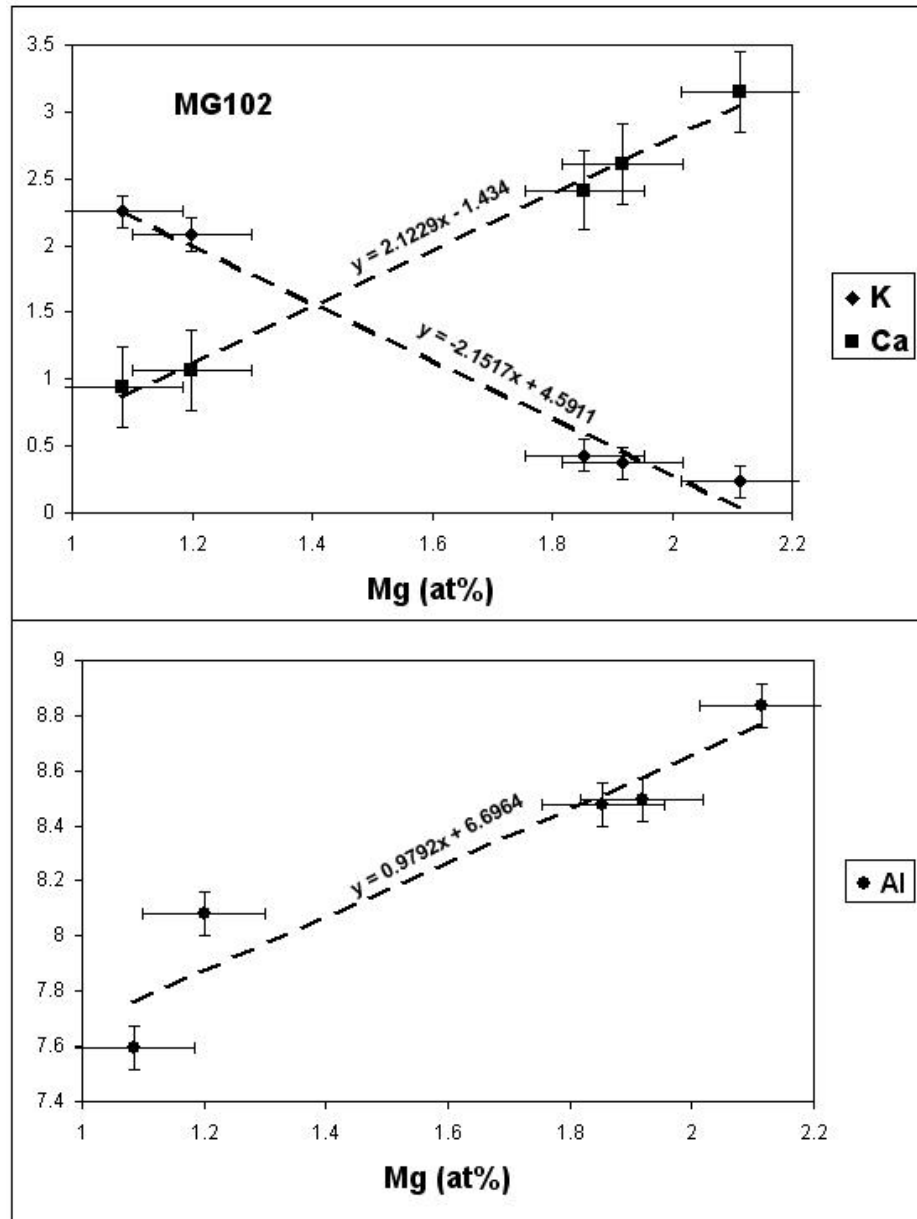


950  
951  
952

|

953  
954

**Figure 10.**



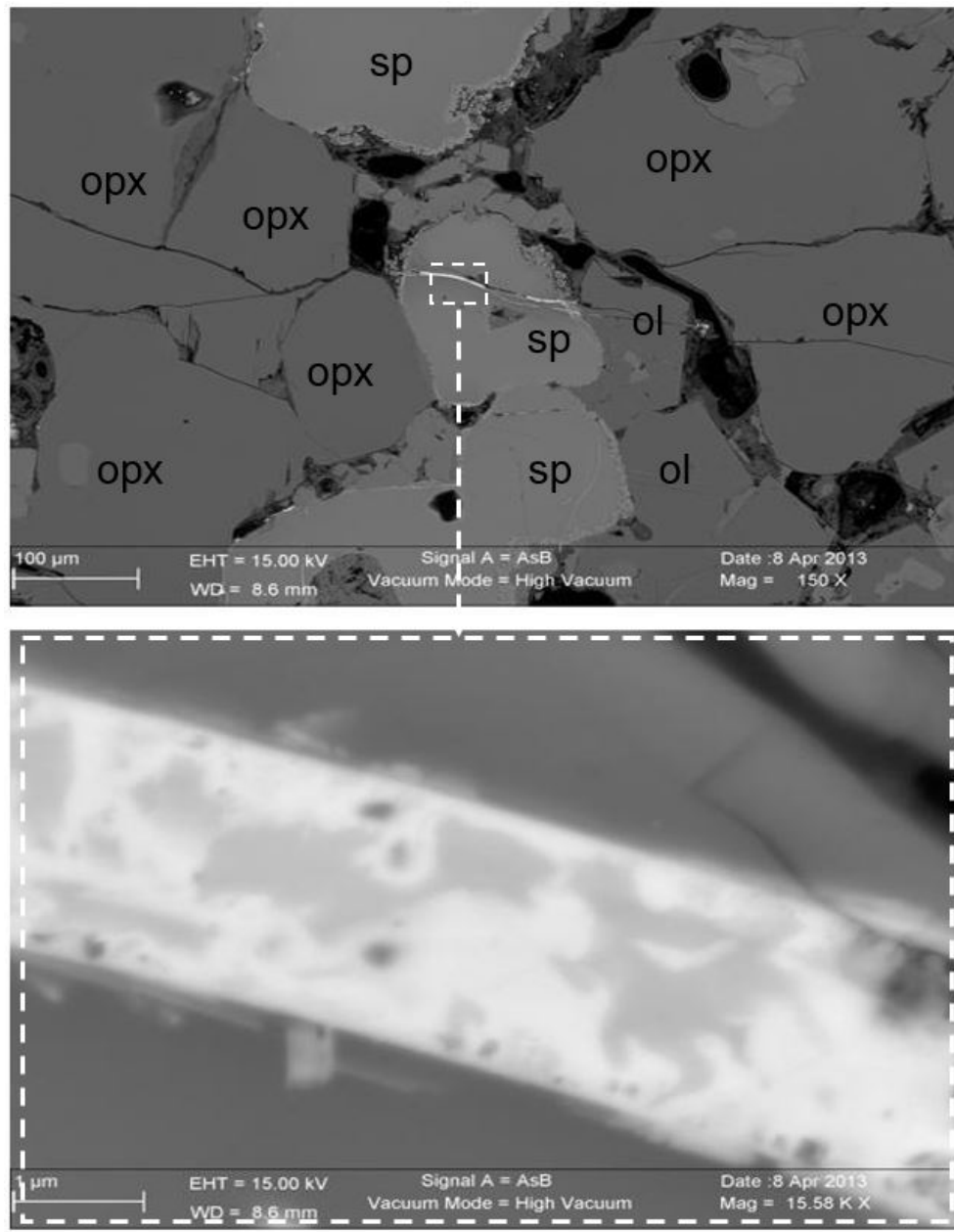
955  
956  
957

|



958  
959

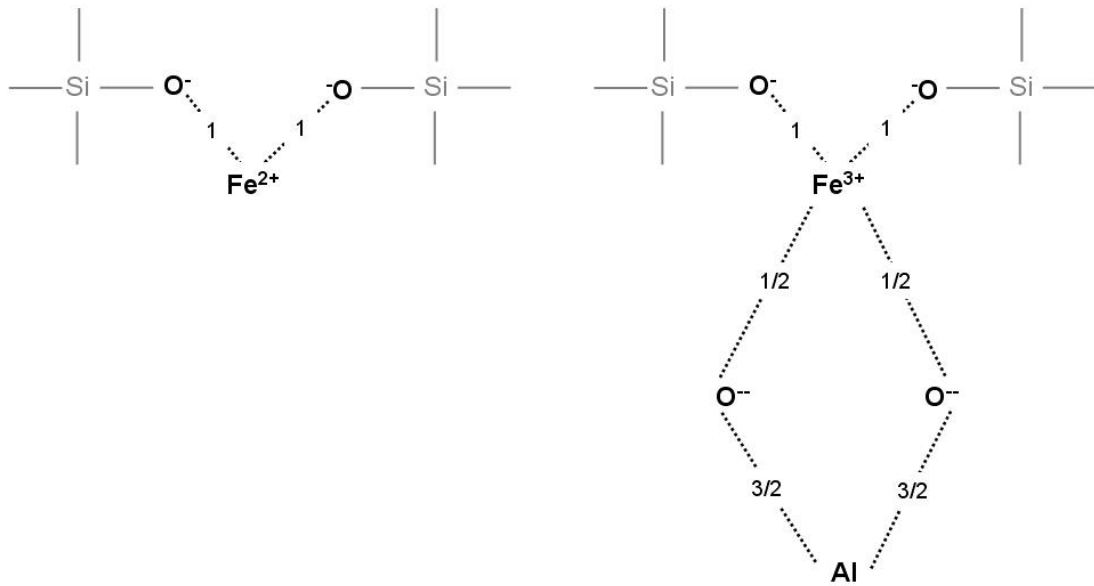
**Figure 11.**



960  
961  
962

963

**Figure 12.**



964

|